Cell adhesion and spreading on fluid membranes through microtubules-dependent mechanotransduction

Oleg Mikhajlov, Ram M Adar, Maria Tătulea-Codrean, Anne-Sophie Macé, John Manzi, Fanny Tabarin, Aude Battistella, Fahima Di Federico, Jean-Francois Joanny, Guy Tran van Nhieu, et al.

Cell adhesion and spreading on fluid membranes through microtubules-dependent mechanotransduction

Oleg Mikhajlov [1,2], Ram M. Adar [1,3]*, Maria Tătulea-Codrean [1,3]*, Anne-Sophie Macé [4,5], John Manzi [1], Fanny Tabarin [1], Aude Battistella [1], Fahima di Federico [1], Jean-Francois Joanny [1,3], Guy Tran van Nhieu [2]†, Patricia Bassereau [1]†

1- Institut Curie, Université PSL, Sorbonne Université, CNRS UMR168, Laboratoire Physico-Chimie Curie, 75005 Paris, France
2- Institute for Integrative Biology of the Cell (I2BC), 1 Avenue de la Terrasse, 91190, Gif-sur-Yvette, France
3- Collège de France, 11 place Marcelin Berthelot, 75005 Paris, France
4- Institut Curie, Université PSL, CNRS UMR144, Paris, France
5- Cell and Tissue Imaging Facility (PICT-IBiSA), Institut Curie, Université PSL, CNRS, Paris, France
*, † - equal contributions

Abstract

During cell adhesion, integrins form clusters that transmit mechanical forces to the substrate (mechanotransduction) and regulate biochemical signaling depending on substrate stiffness. In recent years, mechanotransduction studies significantly advanced our understanding of cell adhesion. Most studies were performed on rigid substrates such as glass, while more physiologically relevant fluid membranes have been less explored. In contrast to rigid substrates, integrins' ligands on fluid supported lipid bilayers (SLBs) are mobile and adhesive complexes cannot serve as anchoring points promoting cell spreading. Here, we demonstrate that cells spread on SLBs coated with Invasin, a high-affinity integrin ligand. We show that in contrast to SLBs functionalized with RGD peptides, integrin clusters grow and mature on Invasin-SLBs to a similar extent as on glass. While actomyosin contraction dominates adhesion maturation on stiff substrates, we find that integrin mechanotransduction and cell spreading on fluid SLBs rely on dynein pulling forces along microtubules, perpendicular to membranes, and microtubules pushing on adhesive complexes, respectively. Our findings, supported by a theoretical model, demonstrate a new mechanical role for microtubules in integrin clustering on fluid substrates. These forces may also occur on non-deformable surfaces, but have been overlooked.

Integrin-mediated adhesion is key to fundamental cellular processes such as cell migration[1], differentiation[2], and the development of tissues and organs[3]. Integrin clusters serve as communication hubs transmitting mechanical forces between cells and substrates. During mechanotransduction, forces generated by a cell and transmitted to a substrate regulate biochemical signaling as a function of substrate stiffness[4].

In recent years, studies on mechanotransduction have brought a wealth of information and conceptual shifts in our understanding of cell adhesion[5]. A plethora of "adhesome proteins" connecting integrins with cytoskeleton was identified and their role in mechanotransduction and cell adhesion was elaborated[6]. The majority of these studies, however, were performed on substrates with immobilized integrin ligands, such as glass or deformable 2D-gels[7]. The actin cytoskeleton plays a crucial mechanical role in adhesion reinforcement on stiff substrates[8]. Actin polymerization is required to form small nascent adhesions (NAs)[9], and actomyosin contraction promotes their growth into large and dense focal adhesions (FAs) connected to stress fibers[10]. However, much less is known about adhesion on soft substrates like 3D matrices[11] or to the plasma membrane of other cells[12], relevant to the interaction between immune and target cells[13,14], where integrin ligands are not immobilized but embedded on fluid membranes.

Supported lipid bilayers (SLBs) are convenient model membranes for mimicking the fluid characteristic of plasma membranes to study cell-cell adhesion[15]. Previous studies with SLBs functionalized with canonical RGD peptides have shown that cells do not spread, nor develop large and dense integrin adhesions like FAs and stress fibers[16,17]. The current understanding is that mobile integrin-ligand complexes on bilayers cannot serve as anchoring points promoting cell spreading as on stiff substrates[10], and NAs cannot reinforce through mechanotransduction to promote strong adhesion on fluid substrates[18]. However, previous studies have not addressed the effect of the integrin receptor-ligand affinity that may significantly differ from RGD peptides and could regulate cell adhesion[19,20].

To directly test the role of integrin receptor-ligand affinity, we used SLBs functionalized with a high-affinity ligand, the *Yersinia* bacterial protein Invasin[21], that binds to a subset of β_1-integrins, including the fibronectin receptor $\alpha_5\beta_1$. On these SLBs, we seeded mouse embryonic fibroblasts (MEF) expressing a recombinant integrin β_1-subunit labeled with a Halotag at its ectodomain in place of the endogenous β_1-integrin[22]. This construct conjugated with membrane impermeable Halotag-dyes allows studying β_1-integrins primarily at the cell surface, excluding signals from integrins inside the cell observed with genetic labeling. We used confocal microscopy to detect β_1-integrin clustering during the time course of adhesion. We quantified cluster areas and integrin densities using fluorescent SLB calibration standards[15] and compared them for Invasin- and RGD-SLBs. Accordingly, we provide evidence for mechanotransduction occurring on Invasin-SLBs, leading to forming FA-like β_1-integrin adhesions. Additionally, we found that cells spread on fluid Invasin- but not on RGD-SLBs. Finally, we show that microtubules but not actin play a significant role in mechanotransduction on these SLBs.

Results

Cell trembling and spreading on SLBs depend on ligands.

SLBs were functionalized with RGD peptides or Invasin, and their fluidity was confirmed by FRAP (Supplementary Fig. S1). Following the addition of MEF cells using brightfield microscopy, we observed cells with fluctuating edges that we called "trembling" as well as "adherent" cells with immobile edges (Fig. 1A; Supplementary videos V1-V2). The fraction of the latter increased over time, reaching 80% on RGD- and Invasin-SLBs after 45 minutes (Fig. 1B). The fraction of "adherent" cells increased faster on RGD- than on Invasin-SLBs (Fig. 1B), possibly due to higher effective RGD densities on SLBs (20,000 RGD/μm^2 vs. 600 Invasin/μm^2) and/or to the RGD binding to a larger range of integrin types that could facilitate integrin activation[23]. To further confirm this, we studied cell adhesion dynamics in the presence of manganese (Mn^{2+}) that activates integrins[24]. Strikingly, integrin activation by Mn^{2+} had no effect on adhesion dynamics on RGD-SLBs. In contrast, it significantly accelerated adhesion on Invasin-SLBs, which had a similar kinetics as on RGD-SLBs (Fig. 1B). While similar cell edge fluctuations were previously reported on glass[25], we found, however, that the adherent proportion on glass remained constant and similar for both ligands with and without Mn^{2+} (Supplementary Figs. S2A-C). These observations suggest that cell adhesion on SLBs but not glass depends on the cell ligand's ability to activate integrins.

Next, we analyzed the morphology of cells spreading on SLBs as a proxy for cell adhesion strength[26] by measuring their "projected areas" on the SLB surface, and their "circularities", which characterize cell shape irregularity (Fig. 1C). Consistent with an early adhesion stage, all "trembling" cells on both ligands had a relatively small and round projected area, independently of Mn^{2+} treatment (Supplementary Figs. S2D-E). Moreover, in agreement with previous studies on fluid substrates[16], we found that fibroblasts did not spread on RGD-SLBs, keeping small projected areas (<200 μm^2) and remaining round ($0.8 < \text{circularity} < 1$), independently of Mn^{2+} treatment (Figs. 1D-E). In contrast, cells spread significantly more on Invasin-SLBs, with median projected areas 1.5- and 2-fold higher than on RGD-SLBs for Mn^{2+}-untreated and treated cells, respectively (Fig. 1E). Surprisingly, 35% of Mn^{2+}-untreated and 75% of Mn^{2+}-treated cells on Invasin-SLBs had irregular shapes with multiple protrusions (circularity < 0.8) and projected areas twice and 3-fold higher than the trembling reference, respectively (Fig. 1C).

Altogether these results indicate that while integrin activation might be a limiting factor on Invasin-SLBs, these can promote cell spreading upon integrin activation by Mn^{2+}, in contrast to RGD-SLBs.

β_1-integrin clusters are denser and larger on Invasin- than on RGD-SLBs.

We used confocal microscopy to study clustering of β_1-integrins, labeled with Alexa488-Halotag ligands, at the cell-SLB interface during the first hour of adhesion. For both RGD- and Invasin-SLBs, we observed the formation of β_1-integrin clusters with isotropic shapes, morphologically different from FAs or actin-dependent podosome-like structures, mainly composed of β_3-integrins (Pr. Cheng-Han Yu, private communication), and contrary to β_1-integrin clusters, formed at low actomyosin contractions[17]. We applied fluorescence calibration to determine integrin

density maps (Supplementary Fig. S3), and image segmentation programs to detect integrin clusters and measure their areas (σ) and densities of integrins (ρ) (Methods). Specifically, we segmented integrin density maps with a threshold of 300 integrins/μm^2, corresponding to the minimal spacing of 58 nm between integrin-ligand pairs observed during mechanotransduction on glass[27].

We observed that 45 minutes after cell seeding, clusters on Invasin-SLBs occupied larger areas and were denser than on RGD-SLBs independent of Mn^{2+} (Figs. 2B-D). Median densities of integrins per cell (ρ) reached about 100 integrins/μm^2 for trembling cells for both ligands (Fig. 2B; Supplementary Figs. S4A-B). However, for adherent cells, median ρ increased significantly higher than for trembling cells: up to 160 integrins/μm^2 and 450 integrins/μm^2 on RGD- and Invasin-SLBs, respectively. Noteworthy, ρ was significantly higher for Invasin- than RGD-SLBs, reaching values comparable to glass[28], that were never observed for RGD-SLBs (Fig. 2B). Moreover, individual integrin clusters were more than twice denser on Invasin- than on RGD-SLBs, with mean values equal to 300 integrins/μm^2 and 125 integrins/μm^2 on Invasin and RGD, respectively (Fig. 2C). Additionally, we compared areas of dense integrin clusters σ_{300}, corresponding to $\rho > 300$ integrins/μm^2 (Fig. 2D). Independent of Mn^{2+} treatment, σ_{300} per cell was significantly higher on Invasin-SLBs, with 23% of clusters larger than the theoretical diffraction limit, DL (183 nm; Methods), as opposed to only 9% for RGD-SLBs (Fig. 2E).

Finally, we found that high integrin densities in integrin clusters correlated with high spreading area and low cell circularity (Figs. 2F-G; Supplementary Fig. S4C). The growth of adhesion clusters and increased cell spreading suggests that mechanotransduction takes place on Invasin-SLBs.

FA proteins are recruited to β_1-integrin clusters.

Integrin clusters grow and mature during cell adhesion on rigid substrates, recruiting FA proteins in response to mechanotransduction driven by actomyosin contractility[6,29]. To determine whether β_1-integrin adhesive clusters could also mature on SLBs, we quantified the recruitment of FA proteins (Figs. 3A-B). "Early adhesion proteins" like talin, kindlin-2, paxillin, vinculin and "late adhesion proteins" like VASP and zyxin were recruited to β_1-integrin clusters both on Invasin- and RGD-SLBs. Except for talin, however, we observed a higher enrichment of all FA proteins on Invasin- than on RGD-SLBs, consistent with higher mechanical forces applied on Invasin-bound cells.

While integrin-mediated mechanotransduction on glass is generally associated with the actin cytoskeleton, microtubules can stabilize and regulate protein turnover in FAs[30,31]. We first measured the association of F-actin to β_1-integrin clusters in MEF cells using lifeact-mScarlet (Fig. 3C). We found actin enrichment at β_1-integrin clusters for both ligands but did not observe actin stress fibers usually associated with mechanotransduction (Figs. 3C; 3E). Furthermore, we found that F-actin was more enriched at integrin adhesion clusters on RGD- than Invasin-SLBs (Fig. 3C). These results contrast with the difference in the enrichment of FA proteins at these structures and suggest that actin does not drive FA maturation on Invasin-SLBs. We then investigated the role of the microtubule cytoskeleton using EMTB-iRFP. We found that microtubules were organized in similar networks at the adhesion interface on SLBs and glass (Supplementary Fig. S5A). However, microtubules were enriched

with a 17% higher median at β_1-integrin clusters (Fig. 3D), with a 17% higher median enrichment on Invasin- as compared to RGD-SLBs, suggesting their involvement in maturation. Moreover, we observed that adaptor proteins that connect talin to microtubules (Kank1[32] and ELKS[33]) were recruited to β_1-integrin clusters (Supplementary Figs. S5C-D).

Dynein pulling along vertical microtubules leads to mechanosensitive growth of integrin clusters.

During mechanotransduction, integrin clusters are subjected to cellular mechanical forces that significantly increase in magnitude if applied against rigid substrates[10]. On fluid SLBs, lateral components of the forces are negligible compared to glass and are only associated with membrane viscosity[34]. However, SLBs can resist higher magnitude normal forces leading to the maturation of integrin clusters. These normal forces might lead to coupled local deformations of SLBs and cell plasma membranes. We observed such deformations while imaging β_1-integrin clusters above the SLB focal plane (Fig. 4A; zoom 1; $0 < z < 1.5$ µm). Akin to clusters at SLB surfaces (Fig. 4A; zoom 2; $z = 0$), clusters in the cell volume had a larger total area in cells on Invasin- than on RGD-SLBs (Fig. 4B). Some of them were associated with membrane tubes that were pulled out of SLBs (Fig. 4A; zoom 2). The proportion of cells with tubes and the number of tubes per cell were significantly higher on Invasin than on RGD (Fig. 4C). These results are consistent with the notion that integrin clusters on Invasin-SLBs are exposed to higher mechanical forces than those on RGD-SLBs, leading to their growth in size and density, higher recruitment of FA proteins and more tubes.

To characterize the origin of vertical forces pulling on integrin clusters, we tested the effects of inhibitors of cytoskeleton polymerization and associated motors on the proportion of cells with tubes and the number of tubes per cell on Invasin-SLBs since they have a higher number of tubes compared to the ones on RGD-SLBs (Fig. 4D; Supplementary Fig. S6A). We found that preventing actomyosin contractility by Rho kinase inhibition (Y-27632) or blebbistatin did not influence the frequency of tube formation, in agreement with previous studies on RGD-SLBs[35]. Y-27632, however, led to a significant decrease in β_1-integrin cluster size and density (Figs. 4E-F). Inhibition of formins and the Arp2/3 complex that nucleate actin polymerization using SMIFH2 and CK666, respectively, also did not affect tube formation frequency (Fig. 4D; Supplementary Fig. S6A). Together, these results suggest that the actin cytoskeleton is not involved or is not the only driver of vertical forces applied on integrin clusters on SLBs.

Microtubules and associated molecular motors were reported to be involved in the mechanosensitivity of FAs on rigid substrates[36,37]. We thus investigated whether they could be involved in tubular deformations of SLBs. We observed dense and large integrin clusters at the SLB surface and on tubes associated with microtubules (Figs. 3D; 4A). When microtubules were depolymerized with nocodazole (NZ) or when dynein activity was blocked with ciliobrevin D (CBD), the frequency and number of tubes decreased drastically (Fig. 4D; Supplementary Fig. S6A). Similar findings were observed in HeLa cells on Invasin-SLBs after dynein inhibition with CBD or silencing of the dynactin subunit p150glued (Fig. 4G; Supplementary Figs. S6B-C). These results suggest that vertical forces applied to β_1-integrin clusters depend on

microtubules and are driven by dynein activity. Finally, NZ and CBD treatment significantly decreased the total area of β_1-integrin clusters and density (Figs. 4E-F). Noteworthy, this NZ effect is opposite to that observed on rigid substrates, where it was described to lead to an increase in size and density of FAs due to enhanced actomyosin contractility when microtubules are depolymerized[38,39].

Globally, these findings suggest that mechanotransduction on SLBs results from the pulling activity of the dynein motors on locally vertical microtubules, leading to the growth and maturation of integrin clusters. Higher microtubule enrichment and higher frequency of tube formation on Invasin- than on RGD-SLBs suggests affinity-dependent mechanotransduction at integrin clusters on SLBs, in contrast with glass. That is consistent with longer lifetime ligand-integrin bonds supporting more efficient mechanotransduction. To further characterize the role of integrin-ligand affinity on integrin clustering on fluid substrates, we propose a theoretical model (Supplementary Material) that supports that ligand-receptor pairs with higher affinity form clusters of larger density and can sustain larger vertical forces (Supplementary Fig. S7).

The model takes into account the concentrations of ligands, receptors, and bonds (i.e., bound ligand-receptor complexes), as well as the average distance between the cell membrane and SLBs. SLB fluidity allows for ligand (and possibly bond) mobility, which plays a dual role in the theory. First, ligand diffusion acts as a chemical contact with a reservoir and promotes cluster formation. Second, the large tangential forces exerted by the cytoskeleton tend to displace bonds rather than break them. Hence, the vertical cytoskeletal forces are the primary driver of mechanotransduction in the theory. We consider adhesion clusters as dense phase-separated regions of bonds. Phase separation is driven by the interplay between diffusion and attractive bond-bond interactions via two mechanisms. The first attractive mechanism is mediated by the membranes[40–42] and the second by adaptor proteins in the adhesion site[43–45]. Cytoskeletal forces drive conformational changes in adaptor proteins and increase the effective attraction between bonds (e.g., via the exposure of vinculin binding sites on talin[46,47]). The formation of adhesion sites depends on affinity and vertical cytoskeletal force in the following way: forces increase the bond-bond attraction, and affinity increases the total number of bonds (Supplementary Fig. S7). The system is predicted to phase separate for sufficiently numerous bonds and strong attraction, implying adhesion clusters. The phase diagram obtained from the model agrees with our experimental results of cell spreading on SLBs, for which the model explains the differences in clustering between the two ligand types (Supplementary Fig. S7).

Integrin clusters are pushed to the cell periphery in a dynein- and microtubule-dependent manner.

Cell spreading correlates with integrin clustering due to mechanotransduction on glass and high viscosity RGD-SLBs[34]. Similarly, we found that for Mn^{2+}-treated cells adhering on Invasin-SLBs, there was a correlation between cell spreading and the presence of membrane tubes, consistent with mechanotransduction at integrin clusters on SLBs (Fig. 5A).

On glass, growing and maturing FAs move from the cell periphery towards the cell center serving as platforms for cell protrusions nucleating F-actin at the cell periphery[48]. FAs also constitute holding points as cells protrude over them during cell polarization[48], a function that they are unlikely to perform on fluid SLBs.

Unexpectedly, we observed that cells formed protrusions on Invasin-SLBs, leading to their symmetrical spreading without polarization (Fig. 1C). In order to investigate this peculiar spreading, we localized β_1-integrin clusters and membrane tubes in cells with respect to the proximity to cell protrusions (Fig. 5B). We found that tubes were more frequent at the cell periphery than at the cell center (Fig. 5C). Furthermore, cells with β_1-integrin clusters in the cell center were significantly less spread and more circular than cells with β_1-integrin clusters at the cell periphery at the base of actin-rich protrusions (Figs. 3E; 5D-E). These results, together with the finding that cell spreading correlates with the density of β_1-integrin clusters (Figs. 2F-H), suggest that dense and mature β_1-integrin clusters at the cell periphery play a role in cell spreading.

Because microtubules and dyneins were crucial for integrin cluster growth and densification (Figs. 4E-F), we hypothesized that when oriented parallel to the substrate, they also played a role in the localization of clusters at the cell periphery, in a similar manner as to what was described for cells spreading on glass[49,50]. In line with this, we often observed microtubule accumulation at peripheral integrin clusters, at the base of actin protrusions (Fig. 3E; Invasin). Cell treatment with NZ or CBD decreased integrin clustering (Figs. 4E-F) and completely abolished integrin cluster localization at the cell periphery (Figs. 5F-G). Noteworthy, cells treated with NZ or CBD did not spread (Figs. 5H-I). We interpret this result as a combination of inhibition of microtubule and dynein pushing on adhesion clusters and an increase in actomyosin contractility possibly linked to microtubule depolymerization[39]. Consistent with an antagonistic role of the actin cytoskeleton on cell spreading, inhibition of Rho kinase with Y27632 led to even more spread cells[51] (Figs. 5H-I). Similarly to cells on glass[52] and RGD-SLBs[16], inhibition of formins by SMIFH2 impaired cell spreading on Invasin-SLBs and integrin cluster movement to the cell periphery without significant effects on cluster growth (Figs. 4E-F; 5F-G). These findings suggest that, due to dynein motor activity along microtubules, large and mature β_1-integrin clusters are pushed towards the cell periphery, contributing to cell spreading on SLBs through actin-rich protrusions emanating from these adhesive clusters.

Discussion

Our understanding of FAs is based primarily on studies on rigid substrates such as glass, where mechanotransduction is mainly driven by actomyosin-dependent forces transduced by actin fibers tangential to the cell basal membrane[53]. Living tissues, however, cover a wide range of stiffness[5] and, instead of being immobilized, integrin ligands can be present in cell membranes[54,55] where they may diffuse laterally with little constraints and may not exert the range of counter-forces required for "canonical" mechanotransduction. Indeed, when cells adhere on SLBs, the absence of actin stress fibers usually associated with FAs that planar forces on SLBs are negligible compared to glass[56,57].

Using *Yersinia* Invasin as a high-affinity β_1-integrin ligand, we show for the first time that cells adhere, spread, and develop large and dense β_1-integrin clusters on fluid substrates (SLBs), similar to FAs on glass (Fig. 2B)[28]. Contrary to glass, on SLBs, actin-related forces tangential to the plasma membrane do not play a dominant role in integrin adhesion due to substrate fluidity. In addition, instead of enhancing adhesion and spreading[38], microtubule depolymerization strongly inhibits it. We show here that

adhesion maturation on bilayers relies on microtubule-dependent forces perpendicular to the bilayer. We evidenced these forces by observing local SLB deformations/tubes connecting the bilayer and the integrin cluster in the plasma membrane (Fig. 4A). The existence of normal force components at integrin clusters was also reported on RGD-SLBs using DNA-FRET force probes[58], but their origin was not identified.

On glass, microtubules orient vertically[59] and associate with mature FA at the cell periphery via several adaptor proteins[33,36]. Moreover, dyneins that stabilize microtubule plus-ends at the plasma membrane[60] interact with integrin adhesion clusters through paxillin and other FA proteins[61,62]. Here, we present several pieces of evidence supporting a role for microtubules in exerting forces on β_1-integrin clusters, normal to the SLB surface: i, microtubules are enriched at integrin clusters on SLBs (Fig. 3D); ii, microtubule-talin adaptors KANK1 and ELKS are recruited at these clusters (Supplementary Figs. S5D-E); iii, some microtubules have a vertical orientation in association with integrin adhesions (Fig. 4A). In addition, we have evidenced microtubule- and dynein-dependent (but not actin-dependent) local tubular membrane deformations connected to the clusters (Fig. 4D) that could be related to integrin endocytosis. Indeed, active β_1-integrins participate in clathrin-dependent endocytic pathway regulated by Arf6 and Rab5 GTPases that use microtubules as tracks and dynein motors for integrin internalization[63,64]. The tube formation that we observe on SLBs could be viewed as part of that process. Indeed, similar membrane tubulation was reported at invadopodia promoting integrin trafficking[65]. Molecular motors can collectively pull tubes from membranes by distributing the load on a dynamically formed motor assembly, as shown *in vitro* for kinesins[66]. Forces of the order of 60 pN or less are necessary to pull tubes from SLBs on glass[67]. Dimers of dyneins exert forces of the order of 7 pN[68] and can then pull on integrin adhesion complexes. When enough motors accumulate at the extremity of the microtubule, they produce the force required to tubulate together the plasma membrane and the SLB attached to it through the integrin-ligand links. This force induces conformational changes in adaptor proteins leading to integrin clustering, which according to our theoretical model, is more efficient for high-affinity Invasin than RGD. During integrin internalization, these membrane tubes are cleaved by dynamin[69]. However, contrary to glass, a double membrane tube is formed during endocytosis on SLBs, with the SLB membrane in the inner layer surrounded by the cell plasma membrane as an outer layer (Figs. 4A; 6). Such double-layer tubes could resist more dynamin scission, leading to the formation of stable tubes.

On rigid substrates, cells form protrusions to spread. In this process, mature FAs act as anchoring points against which growing actin-rich protrusions push. The ability of cells to spread on glass depends on the density of ligands on the surface, the size of integrin adhesions, and their connection to the cytoskeleton[70]. On SLBs, on the other hand, mature integrin adhesions can move in the adhesion plane upon mechanical stimuli. We show for the first time that cells spread on fluid SLBs coated with the high-affinity ligand Invasin. Our results indicate that integrin adhesion clusters mature on fluid substrates and are sufficiently constrained to serve as holding points to support spreading, likely through their connection with microtubules.

Figure 6 summarizes our observations of cell adhesion on fluid substrates. Microtubules were shown to be essential for cell spreading on relaxed collagen networks and for forming dendritic extensions[71]. On Invasin-SLBs, integrin clusters

are dragged in the SLB plane towards the cell periphery in a microtubule and dynein-dependent manner (Fig. 3E). Since dyneins are involved in the maturation of the adhesions, essential for spreading (Fig. 5A), we cannot distinguish whether some dyneins also push microtubules linked to adhesions parallel to the surface towards the edge[72] or whether microtubule dynamics is responsible for this. This movement is likely antagonized by an inward force due to the actomyosin contraction of the cell cortex[73,74] (Figs. 3E; 5J), leading to stalling of integrin clusters at the cell edge where they serve as anchoring centers from which actin-rich protrusions emanate[71,75]. These protrusions might result from a combination of pushing forces from actin and microtubule polymerization and microtubule pushing through dynein activity. The pushing forces are applied against the centrosome to which microtubules are connected (Supplementary Fig. S5B). Remarkably, in contrast with cells on glass where microtubules are essential for cell polarization[76,77], cells do not polarize on SLBs and conserve their central symmetry despite the central role of microtubules through a mechanism that remains to be characterized.

In HeLa cells on SLBs, we also observed dynein/microtubule-dependent formation of tubes (Fig. 4G), suggesting that mechanotransduction associated with forces normal to the adhesion plane occurs in various cell types. Functionalized SLBs allow to study the early stages of cell adhesion on a fluid interface, which is relevant for cell-cell interactions (i.e., brain cells, immune cells, etc.)[4], but not accessible on substrates like glass or gels. Moreover, functionalized SLBs reveal forces probably at play on stiff substrates that cannot be observed with immobilized ligands. Using this platform, we found a new role for dynein motors and microtubules in integrin adhesion cluster growth and maturation on SLBs. In addition, our experiments and physical modeling show that cell adhesion on a fluid interface can be strongly modulated by the receptor-ligand affinity, in contrast with solid surfaces. That might be used as a selective adhesion strategy by T- or B-cells, in which microtubules and dynein motors are known to be involved in clustering TCR and BCR receptors, respectively[78,79].

Acknowledgments

We thank all laboratory members and collaborators, particularly Jay Groves (UC Berkeley) and Julien Pernier (Institute for Integrative Biology of the Cell) for their help in production of bilayers, Luke Lavis (Janelia Farm) for providing fluorophores, David Calderwood (Yale University) for providing MEF cell lines, Christof Hauck (University of Konstanz), Simon De Beco (Paris Diderot University) and Danijela Vignjevic (Institut Curie) for providing genetic constructs used in the study, Stephanie Miserey-Lenkei (Institut Curie) for the help in immunofluorescence experiments, Rémi Fert and Eric Nicolau for the help at the mechanical workshop, Jost Enninga (Institut Pasteur), Anna Akhmanova, Ana-Suncana Smith (Friedrich-Alexander-Universität), Jean-Baptiste Manneville (Laboratoire Matière et Systèmes Complexes, Paris-Cité University), Kristine Schauer (Institut Gustave Roussy), Pierre Sens, Gaelle Boncompain, Alexandre Baffet, Ryszard Wimmer (all Institut Curie) for insightful discussions. We also acknowledge the experimental support of the Molecular Biology and Cells platform at Institut Curie.

This work was supported by the Institut Curie, the Collège de France, the Institut National de la Santé et de la Recherche Médicale (Inserm) and the Centre National de la Recherche Scientifique (CNRS). We further acknowledge the Nikon Imaging Centre at Institut Curie-CNRS, member of the French National Research Infrastructure France-BioImaging (ANR10-INSB-04). O.M. was funded by the European Union's Horizon 2020 research and innovation program under the Marie Skłodowska-Curie grant agreement No 666003, the ARC foundation, the Labex CelTisPhyBio (Grant ANR-11-LABX-0038, ANR-10-IDEX-0001-02). R.M.A. acknowledges funding from Fondation pour la Recherche Médicale (FRM Postdoctoral Fellowship). P.B. and J.F.J. are members of the CNRS consortium Approches Quantitatives du Vivant, the Labex CelTisPhyBio (ANR-11-LABX0038) and Paris Sciences et Lettres (ANR-10-IDEX-0001-02).

Author contributions

O.M., P.B. and G.T.V.N. conceived the study. P.B. and G.T.V.N. acquired funding and equally contributed to this work. O.M. designed and performed experiments, analyzed data, and wrote the original manuscript. A.S.M. and O.M. developed image analysis programs for integrin cluster. F.D.F, J.M. and O.M. performed cloning, expression, purification and labeling of Invasin. A.B. and F.T generated lentiviral constructs and cell lines used in the study. J.F.J. supervised the theoretical work performed and described in the supplementary material by R.M.A. and M.T.C. who equally contributed to this work. O.M., G.T.V.N. and P.B. reviewed and edited the final manuscript. All authors approved the final manuscript prior to submission.

Competing interests

The authors declare no competing interests.

Bibliography

1. Huttenlocher, A. & Horwitz, A. R. Integrins in Cell Migration. *Cold Spring Harb Perspect Biol* **3**, a005074 (2011).
2. Vogel, V. & Sheetz, M. P. Cell fate regulation by coupling mechanical cycles to biochemical signaling pathways. *Curr Opin Cell Biol* **21**, 38–46 (2009).
3. Bökel, C. & Brown, N. H. Integrins in Development: Moving on, Responding to, and Sticking to the Extracellular Matrix. *Developmental Cell* **3**, 311–321 (2002).
4. Discher, D. E., Janmey, P. & Wang, Y.-L. Tissue cells feel and respond to the stiffness of their substrate. *Science* **310**, 1139–1143 (2005).
5. Iskratsch, T., Wolfenson, H. & Sheetz, M. P. Appreciating force and shape — the rise of mechanotransduction in cell biology. *Nat Rev Mol Cell Biol* **15**, 825–833 (2014).
6. Winograd-Katz, S. E., Fässler, R., Geiger, B. & Legate, K. R. The integrin adhesome: from genes and proteins to human disease. *Nat Rev Mol Cell Biol* **15**, 273–288 (2014).
7. Sun, Q., Hou, Y., Chu, Z. & Wei, Q. Soft overcomes the hard: Flexible materials adapt to cell adhesion to promote cell mechanotransduction. *Bioactive Materials* **10**, 397–404 (2022).
8. Sun, Z., Guo, S. S. & Fässler, R. Integrin-mediated mechanotransduction. *J Cell Biol* **215**, 445–456 (2016).
9. Choi, C. K. *et al.* Actin and alpha-actinin orchestrate the assembly and maturation of nascent adhesions in a myosin II motor-independent manner. *Nat Cell Biol* **10**, 1039–1050 (2008).
10. Bershadsky, A. D. *et al.* Assembly and mechanosensory function of focal adhesions: experiments and models. *Eur J Cell Biol* **85**, 165–173 (2006).
11. Yamada, K. M., Doyle, A. D. & Lu, J. Cell–3D matrix interactions: recent advances and opportunities. *Trends in Cell Biology* (2022) doi:10.1016/j.tcb.2022.03.002.
12. Huveneers, S. & de Rooij, J. Mechanosensitive systems at the cadherin-F-actin interface. *J Cell Sci* **126**, 403–413 (2013).
13. Harjunpää, H., Llort Asens, M., Guenther, C. & Fagerholm, S. C. Cell Adhesion Molecules and Their Roles and Regulation in the Immune and Tumor Microenvironment. *Frontiers in Immunology* **10**, (2019).
14. Rose, D. M., Alon, R. & Ginsberg, M. H. Integrin modulation and signaling in leukocyte adhesion and migration. *Immunological Reviews* **218**, 126–134 (2007).
15. Galush, W. J., Nye, J. A. & Groves, J. T. Quantitative fluorescence microscopy using supported lipid bilayer standards. *Biophys J* **95**, 2512–2519 (2008).
16. Yu, C., Law, J. B. K., Suryana, M., Low, H. Y. & Sheetz, M. P. Early integrin binding to Arg-Gly-Asp peptide activates actin polymerization and contractile movement that stimulates outward translocation. *Proc Natl Acad Sci U S A* **108**, 20585–20590 (2011).
17. Yu, C. *et al.* Integrin-matrix clusters form podosome-like adhesions in the absence of traction forces. *Cell Rep* **5**, 1456–1468 (2013).
18. Glazier, R. & Salaita, K. Supported lipid bilayer platforms to probe cell mechanobiology. *Biochimica et Biophysica Acta (BBA) - Biomembranes* **1859**, 1465–1482 (2017).

19. Springer, T. A. Adhesion receptors of the immune system. *Nature* **346**, 425–434 (1990).
20. Langereis, J. D. Neutrophil integrin affinity regulation in adhesion, migration, and bacterial clearance. *Cell Adh Migr* **7**, 476–481 (2013).
21. Isberg, R. R. & Leong, J. M. Multiple β1 chain integrins are receptors for invasin, a protein that promotes bacterial penetration into mammalian cells. *Cell* **60**, 861–871 (1990).
22. Huet-Calderwood, C. *et al.* Novel ecto-tagged integrins reveal their trafficking in live cells. *Nat Commun* **8**, 570 (2017).
23. Shattil, S. J., Kim, C. & Ginsberg, M. H. The final steps of integrin activation: the end game. *Nat Rev Mol Cell Biol* **11**, 288–300 (2010).
24. Ni, H., Li, A., Simonsen, N. & Wilkins, J. A. Integrin activation by dithiothreitol or Mn2+ induces a ligand-occupied conformation and exposure of a novel NH2-terminal regulatory site on the beta1 integrin chain. *J Biol Chem* **273**, 7981–7987 (1998).
25. Galbraith, C. G., Yamada, K. M. & Galbraith, J. A. Polymerizing actin fibers position integrins primed to probe for adhesion sites. *Science* **315**, 992–995 (2007).
26. Price, L. S., Leng, J., Schwartz, M. A. & Bokoch, G. M. Activation of Rac and Cdc42 by integrins mediates cell spreading. *Mol Biol Cell* **9**, 1863–1871 (1998).
27. Cavalcanti-Adam, E. A. *et al.* Lateral spacing of integrin ligands influences cell spreading and focal adhesion assembly. *Eur J Cell Biol* **85**, 219–224 (2006).
28. Wiseman, P. W. *et al.* Spatial mapping of integrin interactions and dynamics during cell migration by image correlation microscopy. *J Cell Sci* **117**, 5521–5534 (2004).
29. Kanchanawong, P. *et al.* Nanoscale architecture of integrin-based cell adhesions. *Nature* **468**, 580–584 (2010).
30. Stehbens, S. & Wittmann, T. Targeting and transport: How microtubules control focal adhesion dynamics. *Journal of Cell Biology* **198**, 481–489 (2012).
31. LaFlamme, S. E., Mathew-Steiner, S., Singh, N., Colello-Borges, D. & Nieves, B. Integrin and microtubule crosstalk in the regulation of cellular processes. *Cell. Mol. Life Sci.* **75**, 4177–4185 (2018).
32. Bouchet, B. P. *et al.* Talin-KANK1 interaction controls the recruitment of cortical microtubule stabilizing complexes to focal adhesions. *eLife* **5**, e18124 (2016).
33. Lansbergen, G. *et al.* CLASPs attach microtubule plus ends to the cell cortex through a complex with LL5beta. *Dev Cell* **11**, 21–32 (2006).
34. Bennett, M. *et al.* Molecular clutch drives cell response to surface viscosity. *Proceedings of the National Academy of Sciences* **115**, 1192–1197 (2018).
35. Glazier, R. *et al.* DNA mechanotechnology reveals that integrin receptors apply pN forces in podosomes on fluid substrates. *Nat Commun* **10**, 4507 (2019).
36. Rafiq, N. B. M. *et al.* A mechano-signalling network linking microtubules, myosin IIA filaments and integrin-based adhesions. *Nat. Mater.* **18**, 638–649 (2019).
37. Seetharaman, S. *et al.* Microtubules tune mechanosensitive cell responses. *Nat. Mater.* **21**, 366–377 (2022).

38. Bershadsky, A., Chausovsky, A., Becker, E., Lyubimova, A. & Geiger, B. Involvement of microtubules in the control of adhesion-dependent signal transduction. *Curr Biol* **6**, 1279–1289 (1996).
39. Chang, Y.-C., Nalbant, P., Birkenfeld, J., Chang, Z.-F. & Bokoch, G. M. GEF-H1 Couples Nocodazole-induced Microtubule Disassembly to Cell Contractility via RhoA. *MBoC* **19**, 2147–2153 (2008).
40. Komura, S. & Andelman, D. Adhesion-induced lateral phase separation in membranes. *Eur. Phys. J. E* **3**, 259–271 (2000).
41. Bihr, T., Seifert, U. & Smith, A.-S. Nucleation of Ligand-Receptor Domains in Membrane Adhesion. *Phys. Rev. Lett.* **109**, 258101 (2012).
42. Fenz, S. F. *et al.* Membrane fluctuations mediate lateral interaction between cadherin bonds. *Nature Phys* **13**, 906–913 (2017).
43. Geiger, B. & Bershadsky, A. Exploring the neighborhood: adhesion-coupled cell mechanosensors. *Cell* **110**, 139–142 (2002).
44. Schwarz, U. S. & Safran, S. A. Physics of adherent cells. *Rev. Mod. Phys.* **85**, 1327–1381 (2013).
45. Braeutigam, A., Simsek, A. N., Gompper, G. & Sabass, B. Generic self-stabilization mechanism for biomolecular adhesions under load. *Nat Commun* **13**, 2197 (2022).
46. del Rio, A. *et al.* Stretching single talin rod molecules activates vinculin binding. *Science* **323**, 638–641 (2009).
47. Yao, M. *et al.* The mechanical response of talin. *Nat Commun* **7**, 11966 (2016).
48. Partridge, M. A. & Marcantonio, E. E. Initiation of Attachment and Generation of Mature Focal Adhesions by Integrin-containing Filopodia in Cell Spreading. *MBoC* **17**, 4237–4248 (2006).
49. Shakiba, D. *et al.* The Balance between Actomyosin Contractility and Microtubule Polymerization Regulates Hierarchical Protrusions That Govern Efficient Fibroblast-Collagen Interactions. *ACS Nano* **14**, 7868–7879 (2020).
50. Dehmelt, L., Nalbant, P., Steffen, W. & Halpain, S. A microtubule-based, dynein-dependent force induces local cell protrusions: Implications for neurite initiation. *Brain Cell Bio* **35**, 39–56 (2006).
51. Chen, B.-H., Tzen, J. T. C., Bresnick, A. R. & Chen, H.-C. Roles of Rho-associated Kinase and Myosin Light Chain Kinase in Morphological and Migratory Defects of Focal Adhesion Kinase-null Cells*. *Journal of Biological Chemistry* **277**, 33857–33863 (2002).
52. Iskratsch, T. *et al.* FHOD1 is needed for directed Forces and Adhesion Maturation during Cell Spreading and Migration. *Dev Cell* **27**, 545–559 (2013).
53. Burridge, K. & Wittchen, E. S. The tension mounts: Stress fibers as force-generating mechanotransducers. *J Cell Biol* **200**, 9–19 (2013).
54. Marlin, S. D. & Springer, T. A. Purified intercellular adhesion molecule-1 (ICAM-1) is a ligand for lymphocyte function-associated antigen 1 (LFA-1). *Cell* **51**, 813–819 (1987).
55. Elices, M. J. *et al.* VCAM-1 on activated endothelium interacts with the leukocyte integrin VLA-4 at a site distinct from the VLA-4/fibronectin binding site. *Cell* **60**, 577–584 (1990).
56. Livne, A. & Geiger, B. The inner workings of stress fibers – from contractile machinery to focal adhesions and back. *Journal of Cell Science* **129**, 1293–1304 (2016).

606 57. Tojkander, S., Gateva, G. & Lappalainen, P. Actin stress fibers – assembly,
607 dynamics and biological roles. *Journal of Cell Science* **125**, 1855–1864 (2012).
608 58. Brockman, J. M. *et al.* Mapping the 3D orientation of piconewton integrin
609 traction forces. *Nat Methods* **15**, 115–118 (2018).
610 59. Stehbens, S. J. *et al.* CLASPs link focal adhesion-associated microtubule
611 capture to localized exocytosis and adhesion site turnover. *Nat Cell Biol* **16**,
612 561–573 (2014).
613 60. Hendricks, A. G. *et al.* Dynein Tethers and Stabilizes Dynamic Microtubule
614 Plus-Ends. *Curr Biol* **22**, 632–637 (2012).
615 61. Rosse, C. *et al.* Binding of dynein intermediate chain 2 to paxillin controls
616 focal adhesion dynamics and migration. *Journal of Cell Science* **125**, 3733–
617 3738 (2012).
618 62. Redwine, W. B. *et al.* The human cytoplasmic dynein interactome reveals
619 novel activators of motility. *eLife* **6**, e28257 (2017).
620 63. Balasubramanian, N., Scott, D. W., Castle, J. D., Casanova, J. E. & Schwartz, M.
621 A. Arf6 and microtubules in adhesion-dependent trafficking of lipid rafts. *Nat*
622 *Cell Biol* **9**, 1381–1391 (2007).
623 64. Mendoza, P. *et al.* Rab5 activation promotes focal adhesion disassembly,
624 migration and invasiveness in tumor cells. *J Cell Sci* **126**, 3835–3847 (2013).
625 65. Feng, Z. & Yu, C. PI(3,4)P2-mediated membrane tubulation promotes integrin
626 trafficking and invasive cell migration. *Proceedings of the National Academy*
627 *of Sciences* **118**, e2017645118 (2021).
628 66. Leduc, C., Campàs, O., Joanny, J.-F., Prost, J. & Bassereau, P. Mechanism of
629 membrane nanotube formation by molecular motors. *Biochimica et*
630 *Biophysica Acta (BBA) - Biomembranes* **1798**, 1418–1426 (2010).
631 67. Gumí-Audenis, B. *et al.* Pulling lipid tubes from supported bilayers unveils
632 the underlying substrate contribution to the membrane mechanics.
633 *Nanoscale* **10**, 14763–14770 (2018).
634 68. Gennerich, A., Carter, A. P., Reck-Peterson, S. L. & Vale, R. D. Force-induced
635 bidirectional stepping of cytoplasmic dynein. *Cell* **131**, 952–965 (2007).
636 69. Arjonen, A., Alanko, J., Veltel, S. & Ivaska, J. Distinct Recycling of Active and
637 Inactive β1 Integrins. *Traffic* **13**, 610–625 (2012).
638 70. Cavalcanti-Adam, E. A. *et al.* Cell Spreading and Focal Adhesion Dynamics Are
639 Regulated by Spacing of Integrin Ligands. *Biophysical Journal* **92**, 2964–2974
640 (2007).
641 71. Rhee, S., Jiang, H., Ho, C.-H. & Grinnell, F. Microtubule function in fibroblast
642 spreading is modulated according to the tension state of cell–matrix
643 interactions. *Proc Natl Acad Sci U S A* **104**, 5425–5430 (2007).
644 72. Mazel, T. *et al.* Direct observation of microtubule pushing by cortical dynein
645 in living cells. *Mol Biol Cell* **25**, 95–106 (2014).
646 73. Murrell, M., Oakes, P. W., Lenz, M. & Gardel, M. L. Forcing cells into shape: the
647 mechanics of actomyosin contractility. *Nat Rev Mol Cell Biol* **16**, 486–498
648 (2015).
649 74. Rossier, O. M. *et al.* Force generated by actomyosin contraction builds bridges
650 between adhesive contacts. *The EMBO journal* **29**, (2010).
651 75. Manneville, J.-B., Jehanno, M. & Etienne-Manneville, S. Dlg1 binds GKAP to
652 control dynein association with microtubules, centrosome positioning, and
653 cell polarity. *Journal of Cell Biology* **191**, 585–598 (2010).

76. Etienne-Manneville, S. Microtubules in cell migration. *Annu Rev Cell Dev Biol* **29**, 471–499 (2013).
77. Etienne-Manneville, S. & Hall, A. Integrin-mediated activation of Cdc42 controls cell polarity in migrating astrocytes through PKCzeta. *Cell* **106**, 489–498 (2001).
78. Hashimoto-Tane, A. *et al.* Dynein-driven transport of T cell receptor microclusters regulates immune synapse formation and T cell activation. *Immunity* **34**, 919–931 (2011).
79. Schnyder, T. *et al.* B Cell Receptor-Mediated Antigen Gathering Requires Ubiquitin Ligase Cbl and Adaptors Grb2 and Dok-3 to Recruit Dynein to the Signaling Microcluster. *Immunity* **34**, 905–918 (2011).

Figure Legends

Figure 1. MEF cells adhere faster RGD- than on Invasin-coated SLBs, but adhered cells spread more on Invasin- than on RGD-coated SLBs.

A) Brightfield images of an adherent (left) and a trembling (right) cell on Invasin-SLB with corresponding kymographs describing cell edge movements over 2 minutes. Scale bars: 10 µm; 1 µm.

B) Time evolution of fractions of adherent cells on SLBs functionalized with RGD (blue) and Invasin (red) in presence (Mn+, full line) or absence (Mn-, dashed line) of Mn^{2+}. Each data point represents between 42 and 113 cells studied in at least 3 independent biological experiments. A fraction of adherent cells 45 minutes after seeding on SLBs without ligands (Ctrl-, green) in absence of Mn^{2+}. Line scatter plot, mean, SEM.

C) Brightfield images of cells with two different morphologies (I – round; II – not round) on SLBs functionalized with RGD (blue) and Invasin (red). Scale bars: 10 µm.

D-E) Trembling ("Tr", plots on grey background area) and adherent ("Ad", 45 min – 1h after seeding) cells in presence (Mn+) or absence (Mn-) of Mn^{2+} adhering on RGD- (blue) or Invasin-coated (red) SLBs. Data from 44 cells, Nexp=3 (independent experiments) for trembling cells on RGD; 57 cells, Nexp=3 for trembling cells on Invasin (both Mn-); 49 cells, Nexp=3 for cells adhering on RGD (Mn-); 53 cells, Nexp=3 for cells adhering on Invasin (Mn-); 58 cells, Nexp=3 for cells adhering on RGD (Mn+) and 49 cells, Nexp=5 for cells adhering on Invasin (Mn+).

D) Circularity of trembling and adherent cells, based on cell edge detection from brightfield images, 45 minutes after seeding. 2 classes of cell morphologies are indicated: I (circularity > 0.8), II (circularity < 0.8). Box plot.

E) Projected area of the cells described in D. Bar plot, median, 95% CI.

Figure 2. β_1-integrin clusters in MEF cells adhering on SLBs and relationship between their density and cell spreading.

A) Main panels: β_1-integrin density maps, using the "physics" LUT of ImageJ below (cf. Methods for the calibration derived from fluorescence images), showing β_1-integrin cluster organization in cells adhering on SLBs coated with RGD (upper left) and Invasin (upper right). Images are taken at the focal plane of the SLBs. Lower left corners: corresponding brightfield images.
Zoomed panels (white squares on the main panels): regions with β_1-integrin clusters (black arrows).
Bottom: β_1-integrin density profiles along the white rectangles in the zoomed panels.
Scale bars: 5 µm (main panels); 1 µm (zoomed panels).

B-E) RGD-SLB (blue), Invasin-SLB (red). Data from 57 cells, Nexp=3 (independent experiments) for trembling cells on invasin; 44 cells, Nexp=3 for trembling cells on RGD (both Mn-); data from adhering cells 45 min – 1h after seeding : 83 cells, Nexp=4 for cells adhering on Invasin (Mn-); 48 cells, Nexp=3 for cells adhering on RGD (Mn-); 78 cells, Nexp=5 for cells adhering on Invasin (Mn+) and 102 cells, Nexp=4 for cells adhering on RGD (Mn+).

B) Distributions of mean β_1-integrin density per cell in trembling ("Tr", plots on grey background area) and adherent ("Ad") cells in presence (Mn+) or absence (Mn-) of Mn^{2+} adhering on RGD- or Invasin-coated SLBs. Box plot.

C) Histograms of integrin densities in individual clusters in Mn^{2+} treated cells adhering on RGD- or Invasin-SLBs. Data from 11,441 clusters on Invasin and 16,115 clusters on RGD.

D) Distributions of total area of β_1-integrin clusters per cell in presence (Mn+) or absence (Mn-) of Mn^{2+} in cells adhering on RGD- or Invasin-SLBs. Box plot.

E) Distributions of areas of individual β_1-integrin clusters of density higher than 300 β_1-integrins/μm^2 in Mn^{2+}-treated cells adhering on RGD (blue)- or Invasin (red)-coated

SLBs. 75-percentile of σ_{300} per cell distribution: 8-9 μm^2 for Invasin-SLBs and 0.1-0.15 μm^2 for RGD-SLBs. Data from 347 clusters for cells adhering on Invasin and 8,954 clusters for cells adhering on RGD. Box plot.

F-G) Mn^{2+}-treated MEF cells adhering on Invasin-SLB during 0 – 1h after seeding to chambers with clusters of highest $\rho > 500$ (magenta); $300 < \rho < 500$ (green); and $\rho < 300$ β_1-integrins/μm^2 (black). Data from 157 cells studied in at least 3 independent biological experiments (Nexp=3) for $\rho > 500$; 61 cells studied in at least Nexp=3 for $300 < \rho < 500$ and 87 cells studied in at least Nexp=3 for $\rho < 300$.

F) Cell circularity. Box plot.

G) Projected cell area (μm^2). Box plot.

Figure 3. Focal adhesion proteins and cytoskeleton (actin and microtubules) are enriched at β_1-integrin clusters on SLBs.

All cells are Mn^{2+}-treated and imaged 45 min – 1h after seeding in the chamber.

A) Main panels: fluorescence multi-channel images showing β_1-integrin (cyan) and paxillin (magenta) cluster organization in cells adhering on SLBs coated with RGD (blue frame, left) and Invasin (red frame, right). Images are taken as max intensity z projections (in Fiji) of the volume with 1 µm height (z coordinate) centered at the focal plane of the SLB. Upper left corners: corresponding brightfield images.
Medium panels: zooms corresponding to the white squares on the main panels. Regions with β_1-integrin and paxillin clusters.
Bottom: β_1-integrin and paxillin intensity profiles along the lines (white rectangles in the zoomed panels).
Scale bars: 5 µm (main panels); 1 µm (zoomed panels).

B) Enrichment of FA proteins in β_1-integrin clusters in cells adhering on SLBs functionalized with RGD (blue) and Invasin (red) as a mean fluorescence intensity of the FA protein in the region of β_1-integrin clusters divided by the mean fluorescence intensity of the protein in the cell. It was compared with "shuffled" control enrichments (black), enrichment calculated at random pixels instead of β_1-integrin clusters regions. Box plot.
Data for every FA protein from between 108 and 181 cells for the shuffled control (shuffled), between 42 and 87 cells (RGD) and between 56 and 128 cells (Invasin). All the cells are studied in at least 3 independent biological experiments (Nexp).

C) Enrichment of F-actin in β_1-integrin clusters in cells adhering on SLBs functionalized with RGD and Invasin. Box plot.
Data from 143 cells (shuffled), 58 cells (RGD) and 85 cells (Invasin). Nexp=3 at least.

D) Enrichment of microtubule in β_1-integrin clusters in cells adhering on SLBs functionalized with RGD (blue) and Invasin (red). Box plot.
Data from 107 cells (shuffled), 53 cells (RGD) and 54 cells (Invasin). Nexp=3 at least.

E) Fluorescence multi-channel images showing β_1-integrin (yellow), actin (magenta) and microtubules (cyan) in cells adhering on SLBs coated with RGD (blue frame, left) and Invasin (red frame, right). Images are taken in the focal plane of the SLBs. β_1-integrin density, actin and microtubules intensity profiles along the lines (black rectangles in the zoomed panels) are plotted for both cells. Scale bars: 5 µm, 1 µm.

Figure 4. Tube formation at β_1-integrin clusters is driven by microtubules and dynein activity.

All cells are Mn^{2+}-treated and imaged 45 min – 1h after seeding in the chamber on Invasin-coated SLBs.

A) Top panel: fluorescence multi-channel image of a MEF cell showing the SLB labeled with a TR-DHPE lipid, β_1-integrin with Halotag-Alexa488, actin with lifeact-mScarlet and microtubules (MT) with EMTB-iRFP. A brightfield image of the cell is in the upper left corner of the merged image.
Zoomed panels: regions corresponding to white squares 1 and 2 on the main panels. Top: x-y. Bottom: x-z section corresponding the lines in x-y.

Scale bars: 10 µm (main panel); 2 µm (zoomed panel xy); 0.5 µm (zoomed panel xz).
B-C) Data from 78 cells, Nexp=4 on Invasin; 102 cells, Nexp=4 on RGD.
B) Distributions of total area of β_1-integrin clusters per cell at the SLB level and in the volume 1.5 µm above the SLB for MEF cells adhering on RGD- (blue) and Invasin-coated (red) SLBs. Box plots.
C) Histograms of the number of detected tubes per cell in MEF cells adhering on RGD- (blue) and Invasin-coated (red) SLBs.
D) Proportion of MEF cells with tubes. Cells adhere on Invasin-coated SLBs in presence of drugs. Data from 78 cells, Nexp=4 for DMSO; 104 cells, Nexp=4 for CK666; 71 cells, Nexp=3 for SMIFH2; 58 cells, Nexp=3 for CK666+SMIFH2; 72 cells, Nexp=3 for Y27632; 86 cells, Nexp=3 for Nocodazole (NZ); 69 cells, Nexp=4 for Ciliobrevin D (CBD). Bar plot: mean, SEM.
E-F) MEF cells treated with Nocodazole (NZ), Cilibrevin D (CBD) and non-treated (DMSO). Data from 86 cells, Nexp=3 for Nocodazole (NZ); 69 cells, Nexp=4 for Ciliobrevin D (CBD); 78 cells, Nexp=4 for DMSO.
E) Distributions of the mean integrin density per cell. Box plot.
F) Distributions of the total area of β_1-integrin clusters per cell. Box plot.
G) Proportion of HeLa cells with tubes. HeLa cells were treated with siRNA against p150glued, siRNA scramble (as a negative control) and with CBD. Bar plot: mean, SEM. Data from 58 cells, Nexp=3 for DMSO; 56 cells, Nexp=3 for siRNA scramble; 61 cells, Nexp=4 for siRNA p150glued and 50 cells, Nexp=4 for CBD.

Figure 5. Dyneins push integrin clusters along microtubules to the cell periphery resulting in cell spreading on SLB.

All cells are Mn^{2+}-treated MEF cells and imaged 45 min – 1h after seeding to the chamber with Invasin-coated SLBs.
A&C-E) Data from 78 cells, 5 independent experiments.
A) Projected cell area (μm^2) of cells with and without detected tubes. Box plot.
B) Schematic representation of the zones in a spreading cell. Red: actin-rich protrusions (lamellipodia-filopodia); green: cell periphery that corresponds to the band parallel to the cell border (excluding actin-rich protrusions) with a width equal to 10% of the cell size (length of the smallest side of the smallest rectangle containing the cell); grey: cell body, which is the central cell area.
C) Projected cell area (μm^2) of cells that have higher β_1-integrin cluster frequency at the cell periphery or at the cell body. Box plot.
D) Cell circularity of cells that have higher β_1-integrin cluster frequency at the cell periphery or at the cell body. Box plot.
E) Tube spatial frequency distribution (number of tubes per μm^2) in the cell periphery zone vs cell center zone. Box plot.
F) Comparative illustration of integrin cluster distribution for the cells treated with drugs (CK666, SMIFH2, Y27632, NZ, CBD and DMSO for non-treated cells). β_1-integrin density maps (represented with "physics" LUT of Fiji, calibrated bar on the side). Images are taken at the SLBs' plane. Corresponding brightfield images are in the upper right corners. Scale bars: 10 µm.
G-I) Data from 78 cells, Nexp=4 with DMSO; 104 cells, Nexp=4 with CK666; 71 cells, Nexp=3 with SMIFH2; 58 cells, Nexp=3 with CK666+SMIFH2; 72 cells, Nexp=3 with Y27632; 86 cells, Nexp=3 with Nocodazole (NZ); 69 cells, Nexp=4 with Ciliobrevin D (CBD).
G) Ratio of spatial frequencies *P* of integrin clusters in the periphery zone ($P_{periphery}$) to the center zone (P_{center}). Cells with more clusters in the periphery have P>1 and are in the green part of the graph where those with more clusters in the center have P<1 and are in the grey part. Box plot.
H) Projected area (μm^2) of cells treated with drugs. Box plot.
I) Circularity of cells treated with drugs. Box plot.

828

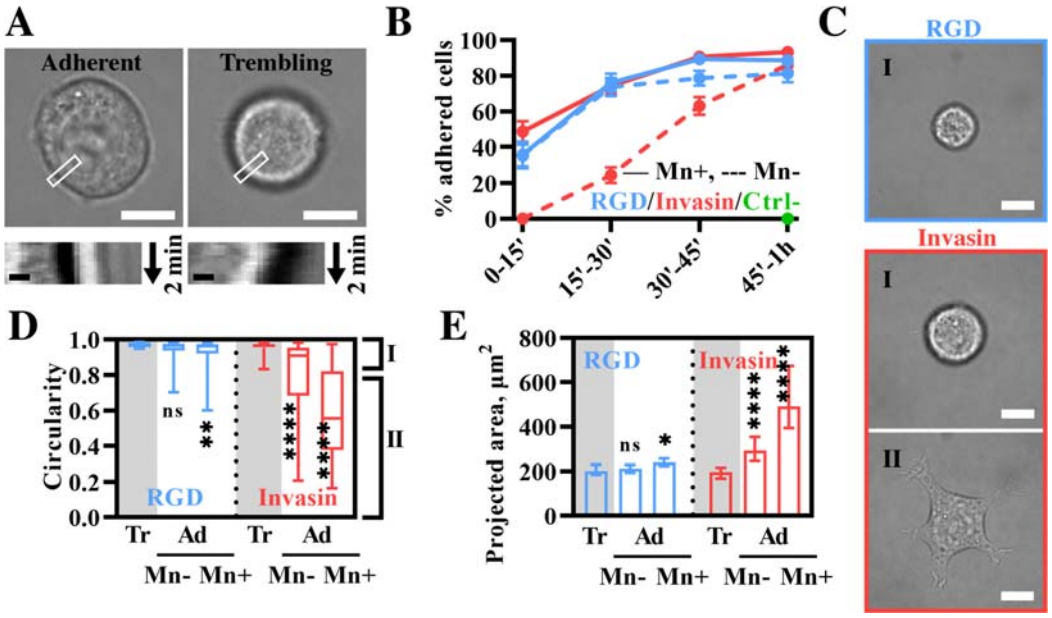

Figure 1. MEF cells adhere faster RGD- than on Invasin-coated SLBs, but adhered cells spread more on Invasin- than on RGD-coated SLBs.

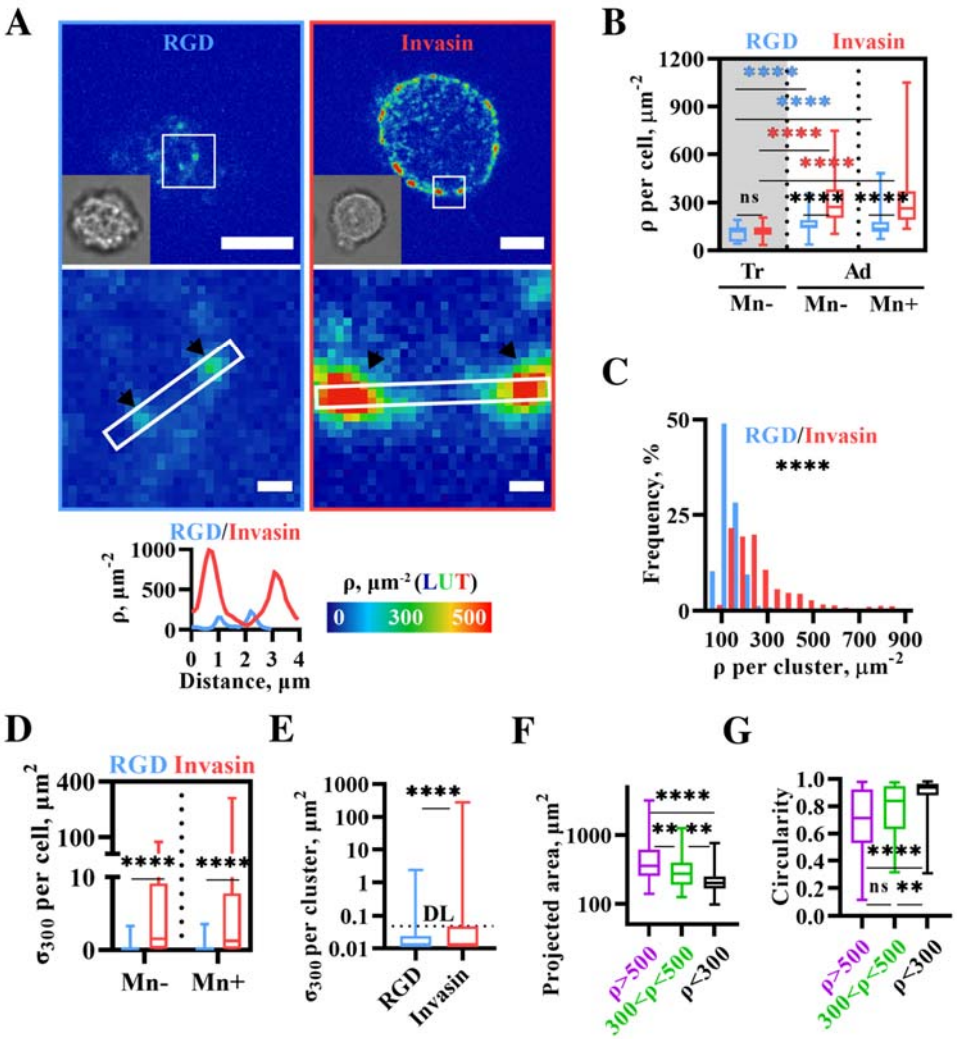

Figure 2. β_1-integrin clusters in MEF cells adhering on SLBs and relationship between their density and cell spreading.

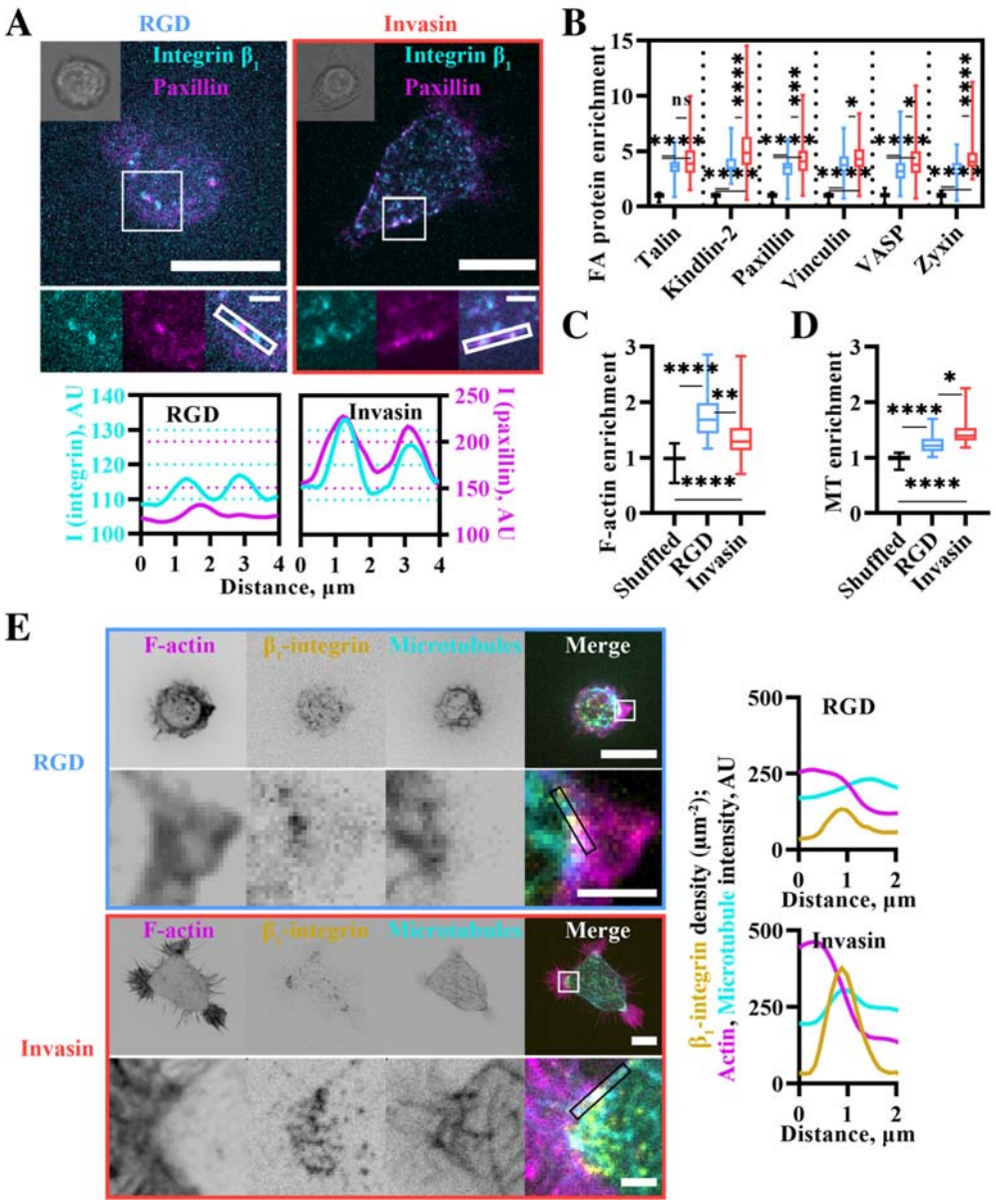

836
837
838 **Figure 3. Focal adhesion proteins and cytoskeleton (actin and microtubules) are**
839 **enriched at β_1-integrin clusters on SLBs.**
840

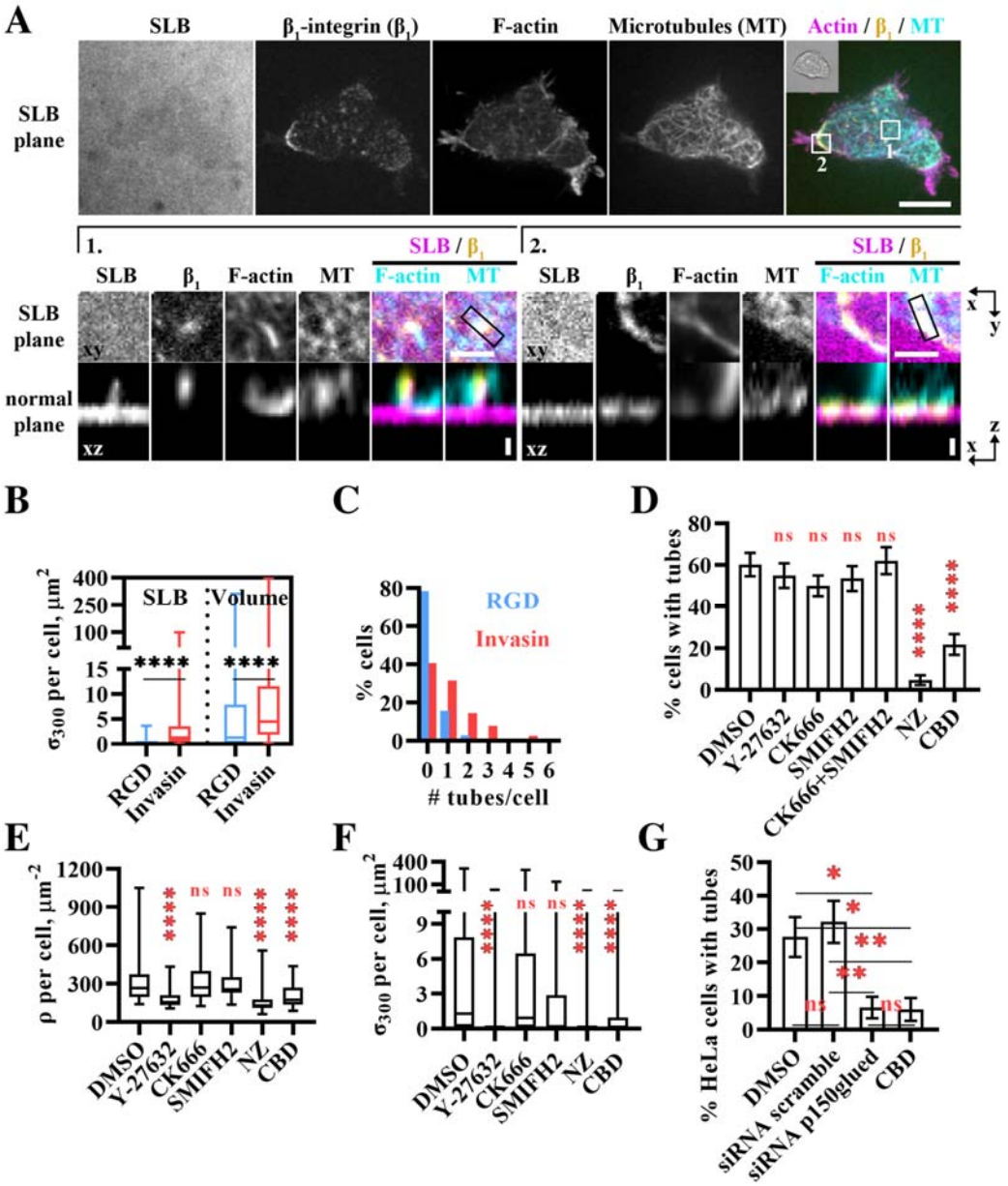

841
842 **Figure 4. Tube formation at β1-integrin clusters is driven by microtubules and**
843 **dynein activity.**
844

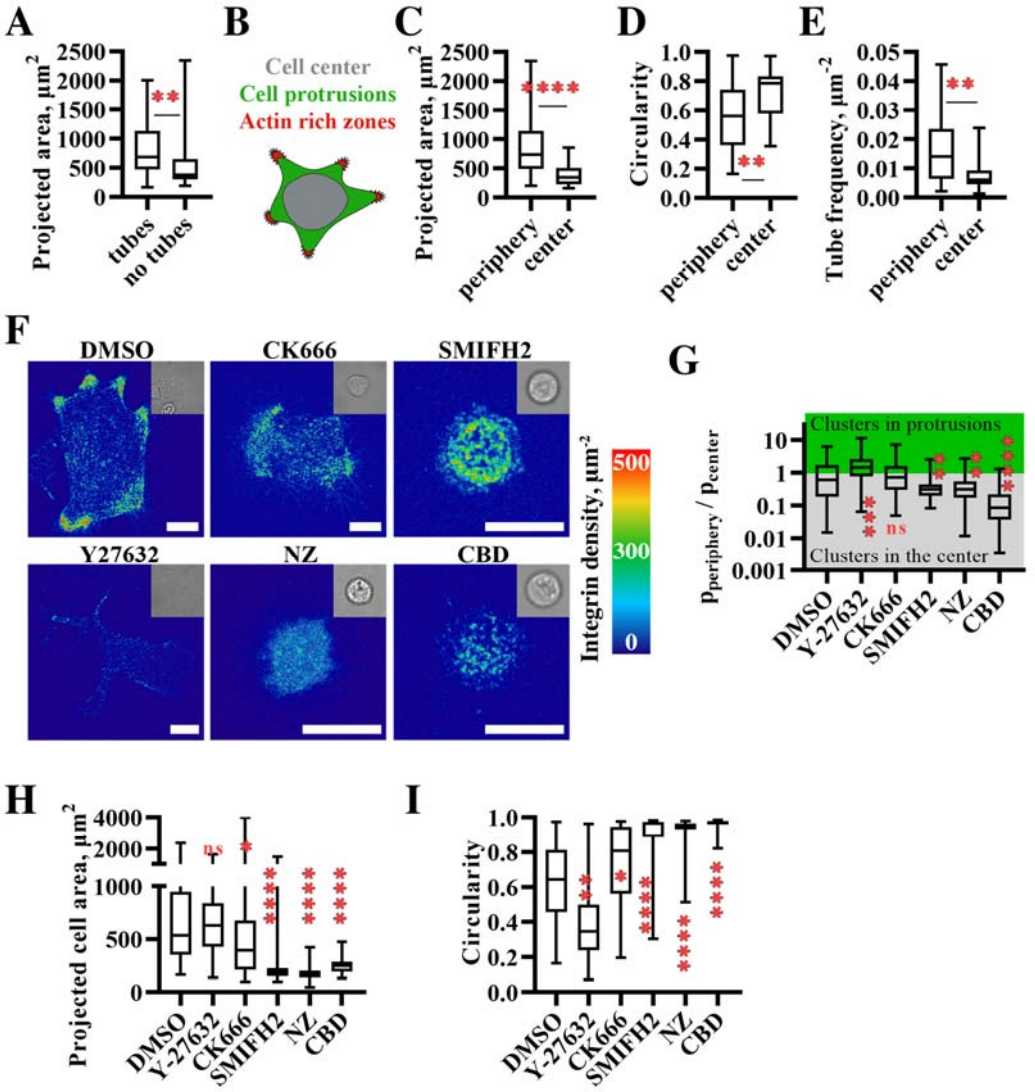

Figure 5. Dyneins push integrin clusters along microtubules to the cell periphery resulting in cell spreading on SLB.

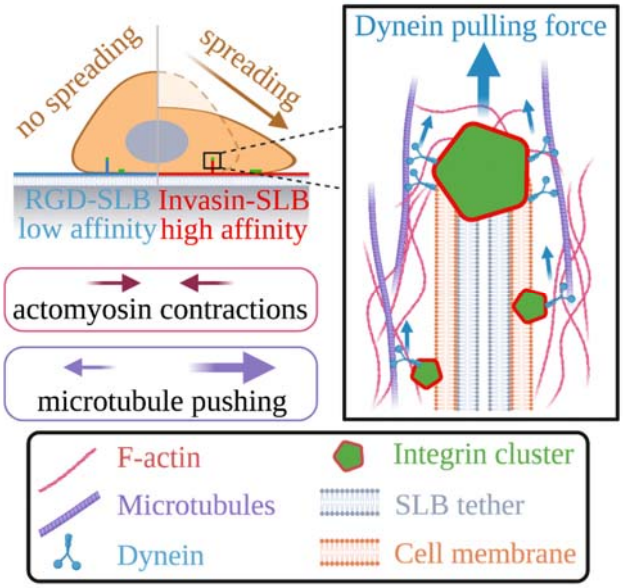

Figure 6. Summary: cell spreading and mechanotransduction during adhesion on SLBs depends on receptor-ligand affinity.

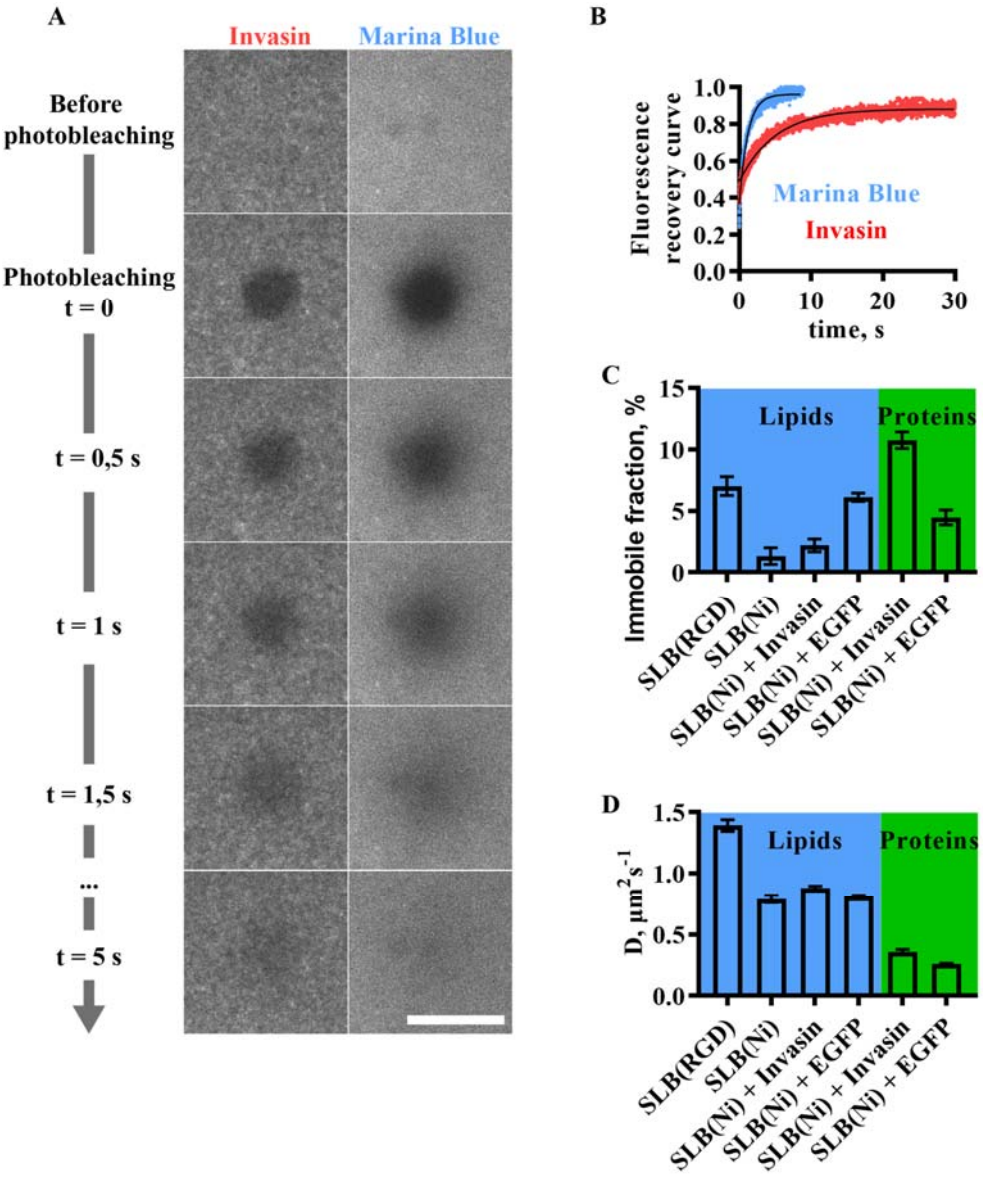

Supplementary Figure S1. SLB fluidity verified with FRAP.

For each sample we have measured 10 FRAP curves in 2 independent experiments from a photobleached circular zone of approximately 20 μm.

A) Illustration of fluorescence recovery after photobleaching. Scale bar: 10 μm.
B) Fluorescence recovery curves normalized by the fluorescence of the neighboring unbleached regions (blue – lipids labeled with Marina Blue, red – Invasin labeled with JF549).
C-D) Different types of SLB surfaces:
C) Immobile fractions of proteins and lipids.
D) Diffusion coefficients of proteins and lipids.

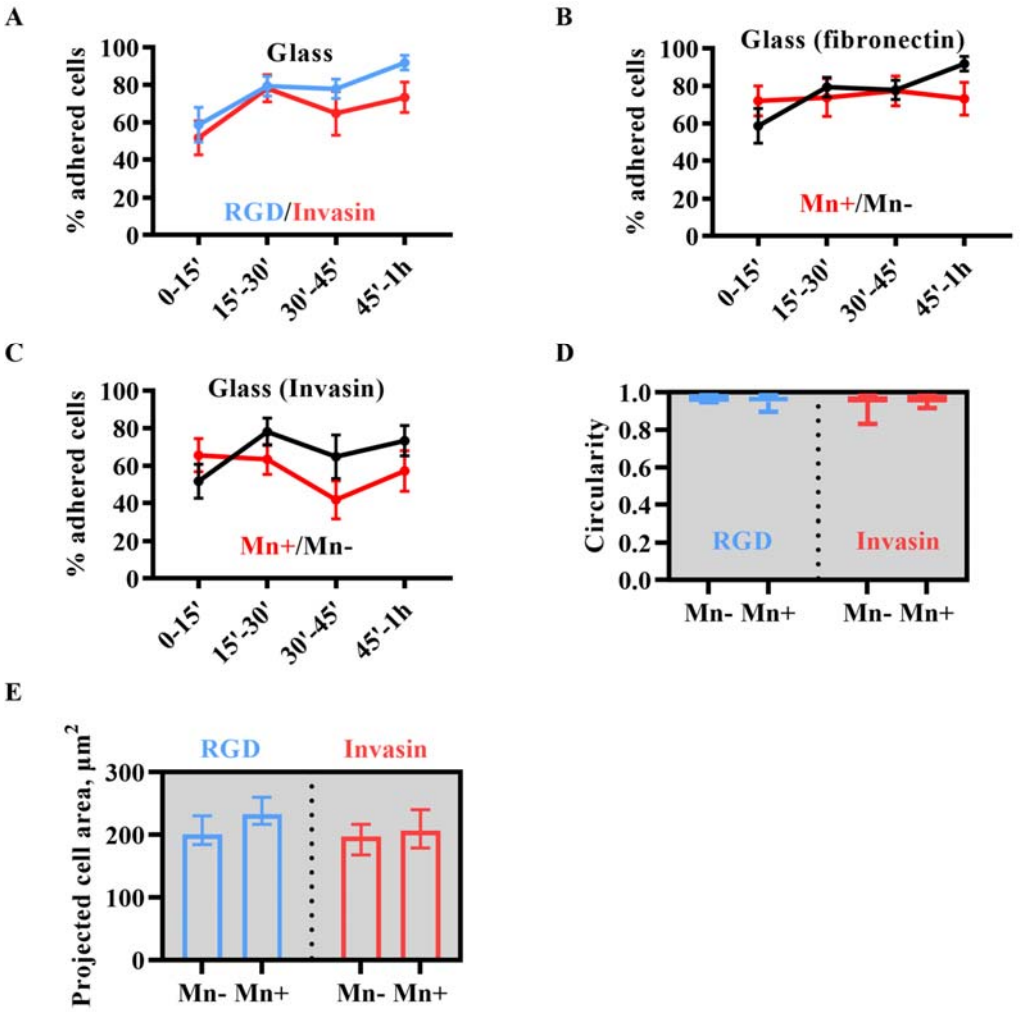

Supplementary Figure S2. Percentage of "adherent" ("non-trembling") MEF cells on glass over time and morphology of "trembling" MEF cells on SLBs.

A-C) Time evolution of fractions of adherent cells on.
For fibronectin (Mn-) each data point represents between 29 and 63 cells studied in at least 3 independent biological experiments (Nexp=3). For fibronectin (Mn+) : between 19 and 32 cells studied in at least Nexp=3. For Invasin (Mn-) : between 17 and 32 cells studied in at least Nexp=3. For Invasin (Mn+) : between 21 and 30 cells studied in at least Nexp=3. Line scatter plots, mean, SEM.
A) glass functionalized with fibronectin (RGD, blue) and Invasin (red) in absence of Mn^{2+}.
B) glass functionalized with fibronectin (RGD) in presence (Mn+, red) and in absence (Mn-, black) of Mn^{2+}.
C) glass functionalized with Invasin in presence (Mn+, red) and in absence (Mn-, black) of Mn^{2+}.
D-E) Cell morphology of "trembling" MEF on SLBs during 1h after seeding to chambers. Data from 44 cells studied in at least 3 independent biological experiments (Nexp=3) for RGD-SLB (Mn-); 35 cells studied in at least Nexp=3 for RGD-SLB (Mn+); 57 cells studied in at least 3 independent biological experiments (Nexp=3) for Invasin-SLB (Mn-); 46 cells studied in at least Nexp=3 for Invasin-SLB (Mn+).
D) Cell circularity. Box plots.
E) Projected cell area. Bar plots, mean, SEM.

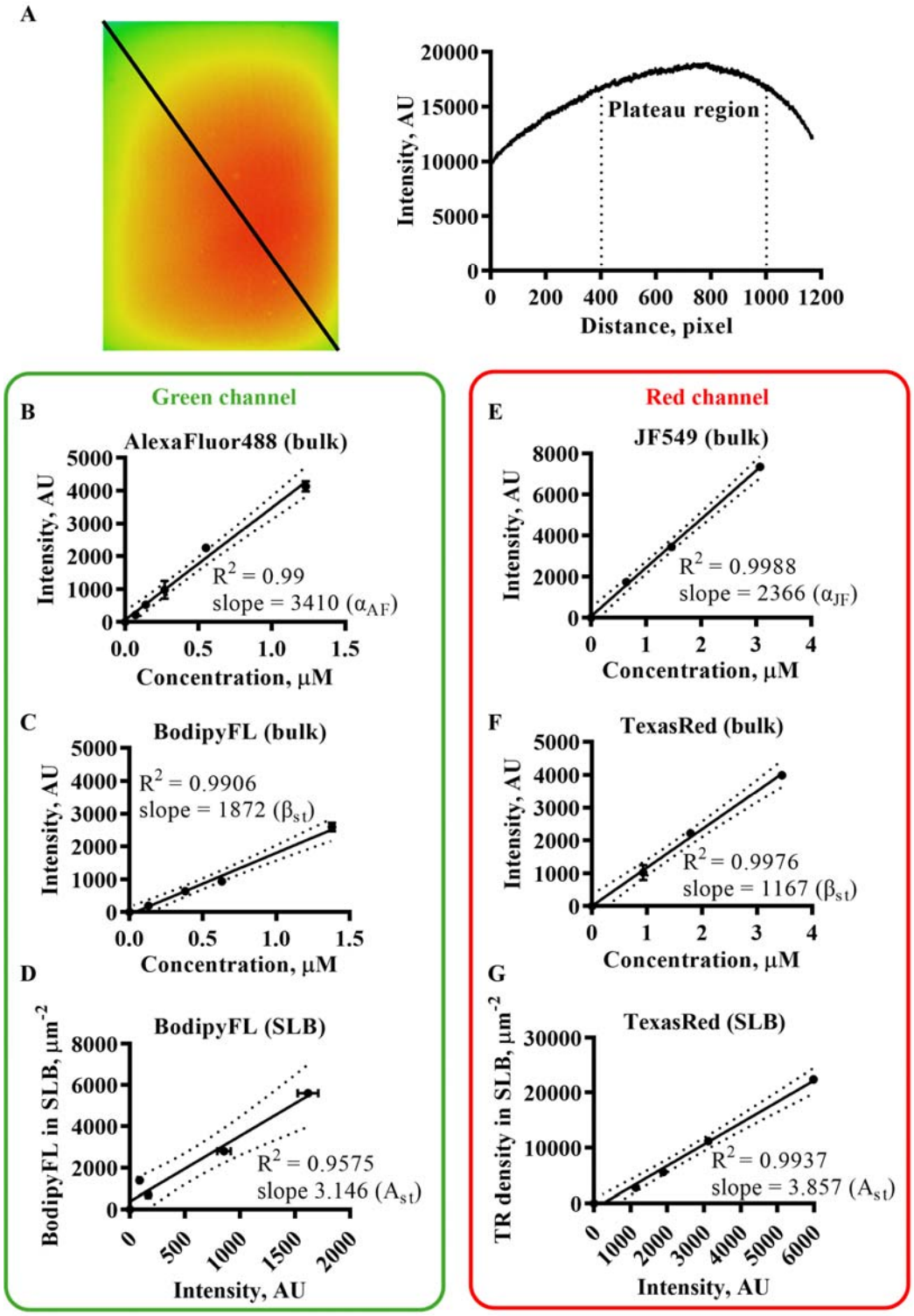

Supplementary Figure S3. Protein density calibration using fluorescence in bulk and on SLBs (Methods).

A) Illumination field (left) and profile along the black line (right) revealed by imaging AlexaFluor 488 dye in bulk solution;
B-D) AlexaFluor488 fluorescence calibration:
B) Fluorescence intensity – concentration curve for AlexaFluor488 in bulk;

C) Fluorescence intensity – concentration curve for BodipyFL in bulk;
D) Concentration – fluorescence intensity curve for BodipyFL on SLB;
E-G) JF549 fluorescence calibration:
E) Fluorescence intensity – concentration curve for JF549 in bulk;
F) Fluorescence intensity – concentration curve for TexasRed in bulk;
G) Concentration – fluorescence intensity curve for TexasRed on SLB.

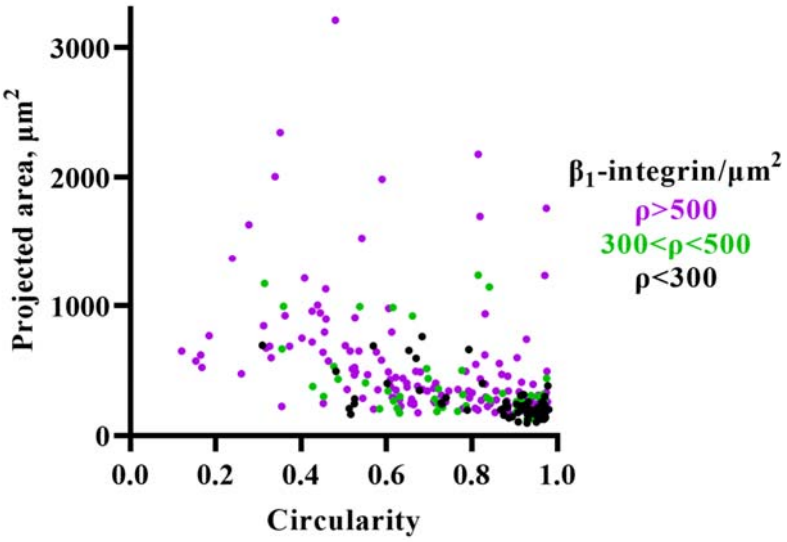

Supplementary Figure S4. Correlation between the maximal β_1-integrin density in the clusters (ρ) and the projected area and the circularity of Mn^{2+}-treated MEF cells on Invasin-SLBs between 0 – 1h after seeding to chambers.

Data from 157 cells studied in at least 3 independent biological experiments (Nexp=3) for ρ >500 ; 61 cells studied in at least Nexp=3 for 300 <ρ < 500 and 87 cells studied in at least Nexp=3 for ρ < 300.

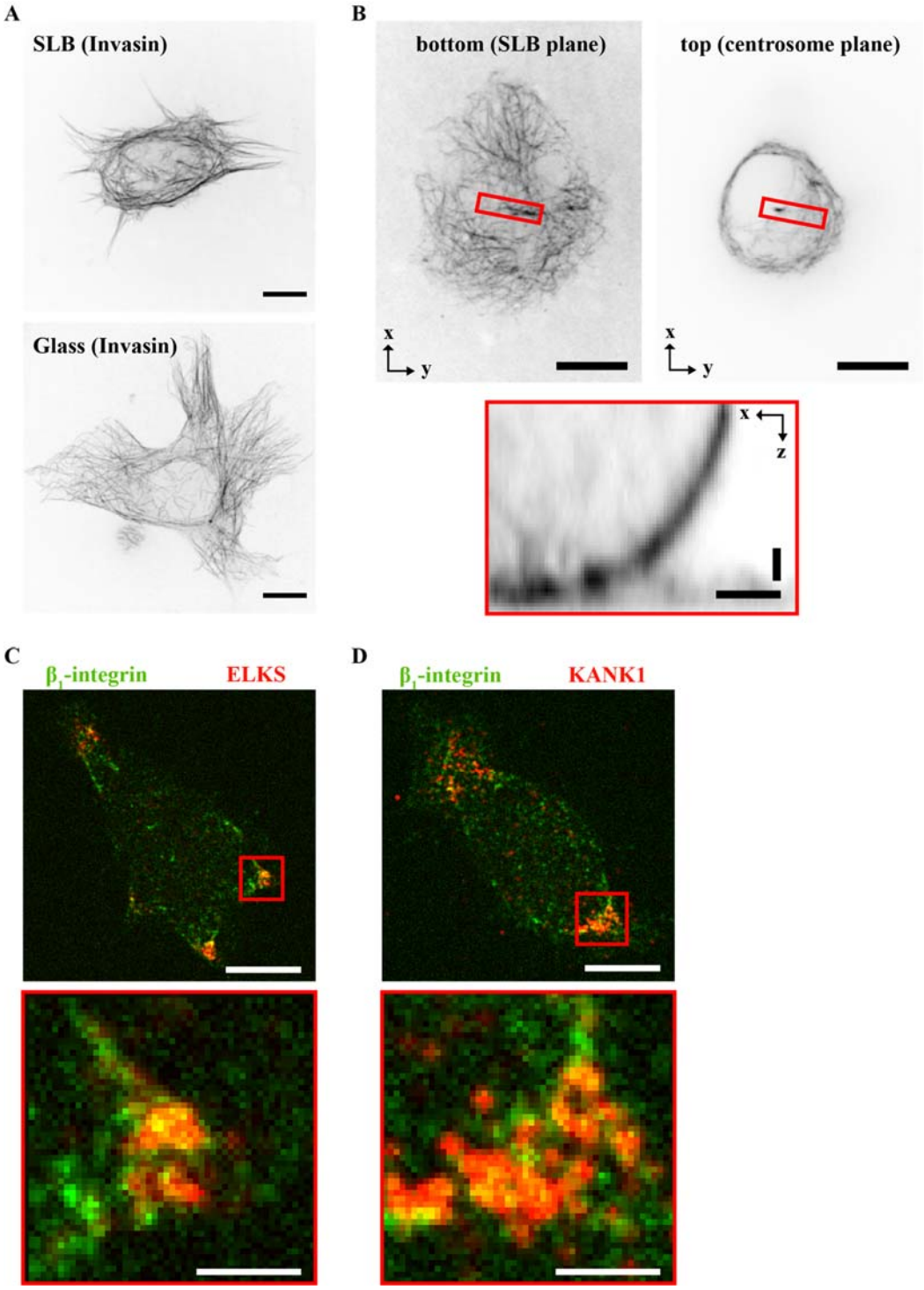

Supplementary Figure S5. Microtubule organization and colocalization of microtubule adaptor proteins with β_1-integrin clusters in MEF cells.

A-B) Microtubules are stained with SiR-tubulin.
A) Distributions of microtubules in the adhesion plane of MEF cells on the SLB (top) and glass (bottom) coated with Invasin. Scale bars: 10 µm.

924 B) Main panels: distributions of microtubules at the SLB plane (top left) and centrosome
925 plane (top right) adhesion plane of MEF cells on an Invasin-SLB. Scale bars: 10 µm.
926 The zoom panel corresponding to the red frames in the main panels (bottom) containing a
927 centrosomal microtubule is shown in the orthogonal to the SLB xz plane. Scale bars: 2 µm
928 (zoomed panel xy); 1 µm (zoomed panel xz).
929 C-D) ELKS (C) and KANK1 (D) (both red) colocalize with β_1-integrin clusters (green) in
930 MEF on Invasin-SLBs. Main panels (top) and zoomed panels (bottom) corresponding to the
931 red frames in the main panels are shown. Scale bars: 10 µm (main panels); 2 µm (zoomed
932 panels).
933

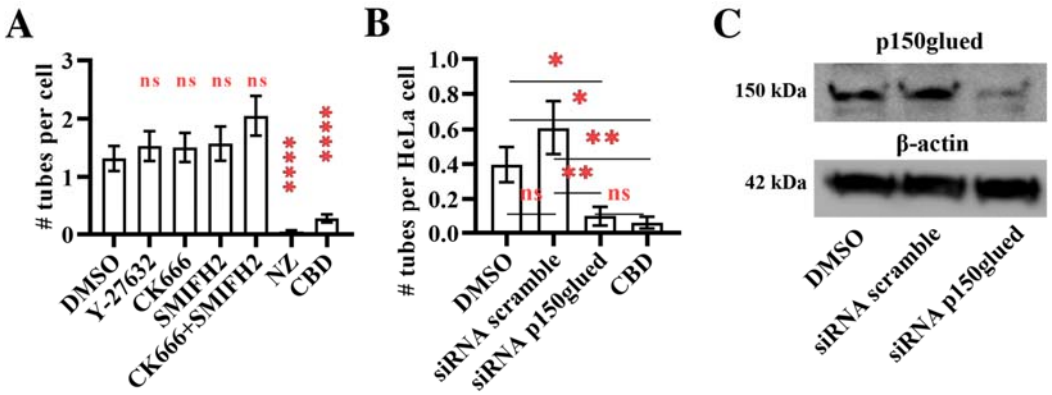

Supplementary Figure S6. Number of tubes per cell (MEF and HeLa) under different treatments (drug inhibitors, siRNA) on Invasin-SLBs.

A-B) Number of MEF (A) and HeLa (B) cells treated with drug inhibitors and siRNA in the presence of Mn^{2+} between 0 – 1h after seeding on Invasin-SLBs. Bar plots: mean, SEM.

A) Data from 78 cells, Nexp=4 with DMSO; 104 cells, Nexp=4 with CK666; 71 cells, Nexp=3 with SMIFH2; 58 cells, Nexp=3 with CK666+SMIFH2; 72 cells, Nexp=3 with Y27632; 86 cells, Nexp=3 with Nocodazole (NZ); 69 cells, Nexp=4 with Ciliobrevin D (CBD).
B) Data from 58 cells, Nexp=3 for DMSO; 56 cells, Nexp=3 for siRNA scramble; 61 cells, Nexp=4 for siRNA p150glued and 50 cells, Nexp=4 for CBD.

C) Representative Western Blots showing a 77% reduction in the expression of p150glued subunit of dynactin in HeLa cells due to siRNA knockdown. Lysates of HeLa cells were prepared 48h after transfection with siRNA. p150glued (top) and β-actin (bottom) protein expression levels were analyzed by Western blotting using antibodies recognizing these proteins.

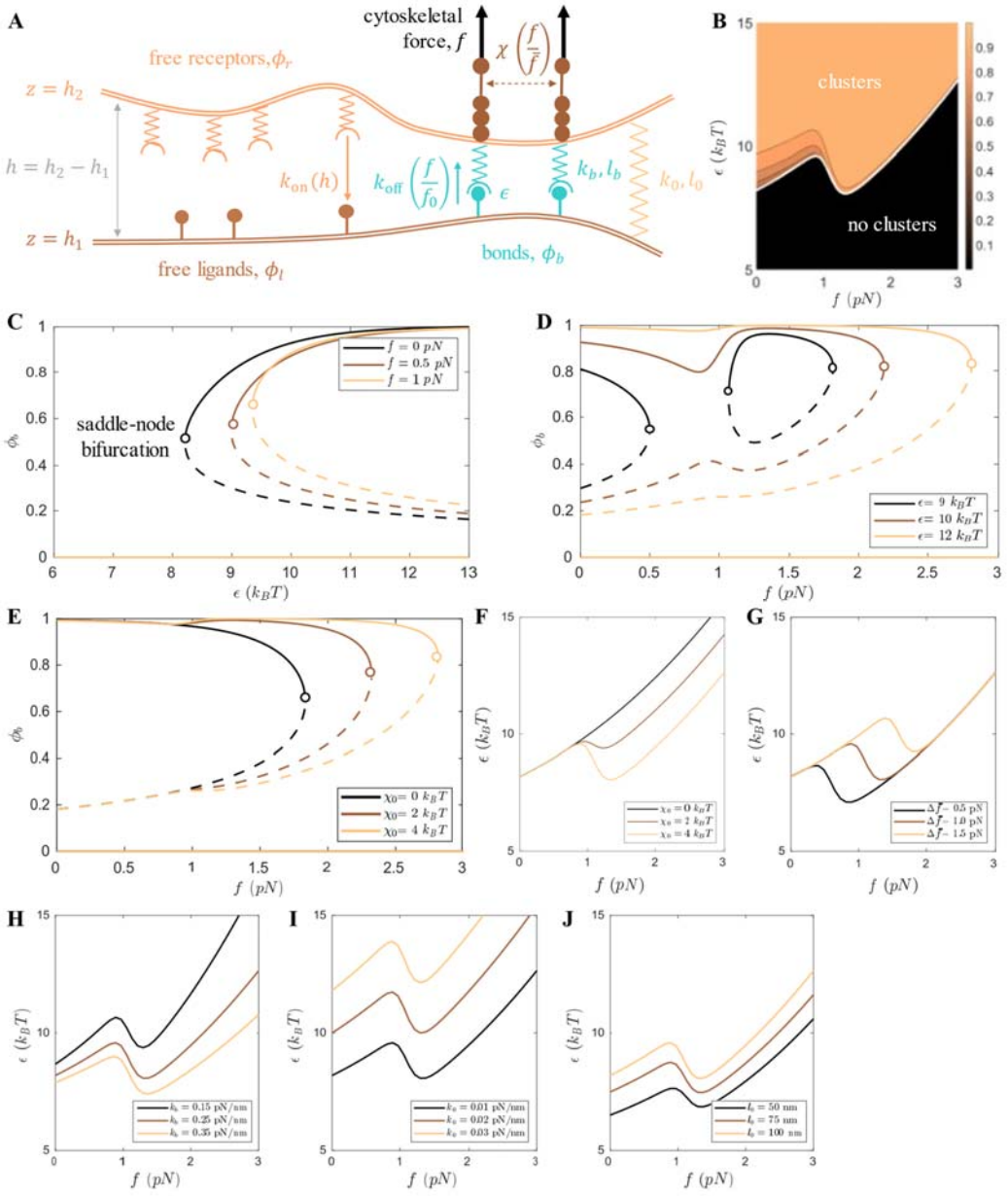

Supplementary Figure S7. Theoretical predictions of integrin clustering as phase separation.

A) Schematic illustration of the model. Free receptors and ligands form bound complexes (bonds) at a rate k_{on} which depends on the distance between the cell membrane and the SLB, $h = h_2 - h_1$. The binding process is characterised by a gain in binding energy, ϵ. Once formed, a bond dissociates at a rate koff that increases when the bond is under force. The cytoskeleton applies a constant force, f, to each bond, which can stretch the adaptor proteins (force scale $\bar{f}$) or even break the bond (force scale $f_0 > \bar{f}$). The interaction strength, χ, describes the effective attractive interaction between bonds. The bonds are modelled as harmonic springs with rest length l_b and spring constant k_b, while the short-range interaction between cell membrane and SLB is also modelled as a spring of rest length l_0 and spring constant k_0.

B-C) Clustering as phase separation.

B) Phase diagram of the system against the cytoskeletal force per bond, f, and the binding energy, ϵ. Above a critical binding energy (white line), the system can sustain two distinct bond concentrations at steady state, indicating that clusters can form. The color indicates the highest sustainable bond density.
C) Bifurcation diagram of the steady state bond concentration against the binding energy, ϵ. The dilute phase (solid line, $\phi_b \approx 0$) always exists, but a dense phase (solid line, $\phi_b \to 1$) appears above a critical binding energy through a saddle-node bifurcation. The middle solution (dashed line) is always unstable.

D-E) Clustering under force. The clusters can sustain larger forces (i.e. the dense phase persists until a larger cytoskeletal force per bond) for (D) higher affinity ligands (increasing ϵ) or (E) stronger attractive interaction through the adaptor proteins (increasing χ_0). In (E), the value of the binding energy is $\epsilon = 12\ k_B T$.

F-J) Dependence of phase diagram on model parameters. Each subfigure depicts the critical binding energy for clustering (white line in B) for several values of (F) interaction strength of activated bonds, χ_0, (G) force required to activate the bonds, $\Delta\bar{f}$, (H) spring constant of the receptors/bonds, k_b, (I) spring constant of the glycocalyx, k_0, and (J) size of the glycocalyx, l_0.

Supplementary video V1 :
Brightfield time-lapse imaging of a trembling MEF cell on Invasin-SLB. Frames were acquired at an interval of 10 sec and video playback speed is at 7 fps. Time in min:sec. Scale bar: 5 µm.

Supplementary video V2 :
Brightfield time-lapse imaging of an adherent MEF cell on Invasin-SLB. Frames were acquired at an interval of 10 sec and video playback speed is at 7 fps. Time in min:sec. Scale bar: 5 µm.

Methods

Cell chamber assembly

For the bilayer to be always hydrated it is formed in a sample flow chamber that always has buffer inside. The sample chamber for the cell adhesion experiment is a custom-made flow chamber that consists of a 26 mm x 76 mm coverglass slide and a 1.5 thickness coverslip from VWR glued together by two melted stripes of parafilm. Prior to chamber assembly the coverslip is cleaned and activated in a series of sonication steps of 30 min in the water bath sonicator (Elmasonic S 10 (H)): in distilled water, 2% Hellmanex III, distilled water, 1M KOH, distilled water. The KOH has a dual role of cleaning and glass activation. At the end of the cleaning steps the coverslip is dried under nitrogen flow and assembled to form the microscopy chamber. Coverglass slides are simply rinsed with EtOH, H20, EtOH and blow dried with nitrogen.

The distance between the two glass slides (the height of the channel) is about 250 µm. The chamber volume is about 50 µl. The assembled chambers can be stored in closed Petri dishes (protected from dust) at room temperature for about 3 days.

Small Unilamellar Vesicles (SUVs) preparation

1,2-dioleoyl-*sn*-glycero-3-phosphocholine (DOPC), 1,2-dioleoyl-sn-glycero-3-[(N-(5-amino-1-carboxypentyl)iminodiacetic acid)succinyl] nickel salt (DGS-NTA(Ni)), 1,2-dioleoyl-sn-glycero-3-phosphoethanolamine-N-[4-(p-(cysarginylglycylaspartate-maleimidomethyl)cyclohexane-carboxamide] sodium salt (DOPE-RGD) were purchased from Avanti Polar Lipids (Alabaster, AL, USA). Invitrogen™ Marina Blue™ 1,2-dihexadecanoyl-*sn*-glycero-3-phosphoethanolamine (Marina Blue™ DHPE) was purchased from Invitrogen (Waltham, MA, USA). SLBs were formed by fusion of Small Unilamellar Vesicles (SUVs) on the coverslip. We used two lipid compositions to prepare SUVs and consequently SLBs: 1) DOPC/DGS-NTA(Ni)/DHPE-Marina Blue (94/2/4, mol/mol); 2) DOPC/DOPE-RGD/DHPE-Marina Blue (94/2/4). Similar lipid compositions were successfully used by other groups to prepare SLBs[1] (Nye and Groves [2008]). The SUVs were prepared using the following protocol:

1. Lipids solubilized in chloroform are mixed together in a glass vial at 1 mg/ml, blow dried with a nitrogen flow, placed in vacuum desiccator for 1 hour, then rehydrated with distilled water for 15 min at room temperature, to a final lipid concentration of 1 mg/ml;
2. After rehydration, the glass vial is vortexed to detach the liposomes;
3. The solution is sonicated for 30 min in the water bath sonicator (Elmasonic S 10 (H));
4. The solution is then centrifuged at 20k RCF for 1 hour;
5. The solution is filtered through a 200 nm filter (Millipore) with a syringe;
6. The sample is dissolved in the SUV fusion buffer at the final composition: 10 mM Tris pH 7.3; 120 mM NaCl.

Lipids preparations are closed under with argon at all stages of SUV preparation to minimize their degradation by oxidation. The prepared SUVs were not stored but used immediately to prepare SLBs.

Invasin preparation

While RGD-ligands bind to a larger repertoire of integrins ($\alpha_5\beta_1$, $\alpha_8\beta_1$, $\alpha_V\beta_1$, $\alpha_V\beta_3$, $\alpha_V\beta_5$, $\alpha_V\beta_6$, $\alpha_V\beta_8$ and $\alpha_{IIb}\beta_3$)[2] (Humphries2006), Invasin binds to a subset of β_1-integrins ($\alpha_3\beta_1$, $\alpha_4\beta_1$, $\alpha_5\beta_1$ and $\alpha_6\beta_1$), including the fibronectin integrin $\alpha_5\beta_1$, with which Invasin has a dissociation constant (K_d) two orders of magnitude lower than that of RGD peptide[3] (Van Nhieu1991).

- **Plasmid preparation**

The plasmid for invasin expression was constructed in two steps. First, a DNA sequence coding for a TEV cleavage site followed by a 6xHis tag followed by the sequence coding for the last 474 amino acids of Invasin, inv474 (PDB: 1CWV) (in 5 3 direction) and flanked by SacI and HindIII restriction sites was synthetized and subcloned by Thermo Fisher Scientific. Second, the insert of interest was cloned into a pMal p5x expression vector by digesting with SacI and HindIII enzymes and ligation. As a result, we have obtained the plasmid that expresses a periplasmic maltose binding protein (MBP) fused to Invasin in E.Coli periplasm under IPTG inducible P_{tac} promoter (pOM3474).

- **Invasin expression**

For Invasin expression we followed the previously described protocol[4] and expressed Invasin in the *E. Coli* periplasm to insure the oxidizing environment for the proper disulfide bond formation. We used an *E. Coli* strain lacking *DegP* protease[4]. Proteins were expressed in 2YT medium + selection antibiotics (ampicillin for the plasmid and kanamycin for the *E. Coli* strain at final concentrations 100 µg/ml and 50 µg/ml, respectively) + 0.2% glucose. Glucose is needed to inhibit amylase expression that can later perturb MBP-Invasin purification. Bacterial culture was inoculated from a single colony and incubated at 30 °C while shaking until the OD_{600} = 0.5−0.6. Then cells were induced with 0.5 mM IPTG for 4 hours. MBP-Invasin is well expressed at the right molecular size (approximately 96 kDa), thus we can proceed with the protein production, purification and labelling at the bigger scale.

- **Invasin purification**

Invasin purification and labelling was performed in several steps:

1. Affinity purification using an amylose resin (New England Biolabs);

2. MBP cleavage by TEV protease;

3. Protein labeling with a succinimidyl ester (SE, Tocris) reactive dye (optional);

4. Purification by size exclusion chromatography using a Superdex 75 column.

The more detailed protocol illustrates the purification process from 2 liters of bacterial culture that expressed MBP-Invasin:

Cell lysis

1. Resuspend cell pellets in approximately 80 mL Lysis Buffer: 25 mM HEPES pH 7.3, 500 mM NaCl, 1 mM EDTA;

2. Add a final of 1x EDTA Free cOmplete protease inhibitor tablet (Roche), 1 mM PMSF, 10 µg/ml DNase and 10 µg/ml lysozyme;

3. Cells were lysed via sonication (misonix sonicator ultrasonic processor XL, large probe at 20% intensity) on ice at 70% intensity: 3 sec - On, 3 Sec Off for 5 minutes;

4. Sample was centrifuged at 20,000 RCF for 60 Min, 4°C and supernatants collected; Affinity purification against the MBP;

5. 10 mL Amylose Resin were pre-washed in water then Lysis buffer;

6. Cleared extracts were applied to Amylose Resin, and allowed to bind using a tube roller for 2h, 4°C;

7. Samples were washed 2x 40mL using batch method with Wash Buffer 1 (+EDTA);

8. Amylose beads were applied to a column and washed a further 10x CV with the same buffer;

9. Proteins were eluted in 15 mL of Elution Buffer: 25 mM HEPES pH7.3, 500 mM NaCl, 10 mM maltose (the steps of the affinity purification against the MBP were repeated);

10. Protein concentration was estimated by measuring the absorbance spectrum at the Cary Eclipse Fluorescence spectrophotometer; the samples were analyzed by protein electrophoresis on SDS-PAGE gels.

TEV cleavage and labelling with JF549 SE dye

11. Add TEV protease at about 1:100 (TEV/Invasin, mol/mol);

12. Add JF549 SE dye (Tocris) at about 1:2 (Invasin/dye, mol/mol);

13. Incubate at 4°C in aluminum foil on the rolling table o/n; Size exclusion purification;

14. Labelled samples were concentrated down to approximately 500 µL and purified further by size exclusion chromatography using a Superdex 75 column. Buffer: 25 mM HEPES pH 7.3, 120 mM NaCl. The elution fractions were analyzed by protein electrophoresis on SDS-PAGE gels.

The fractions corresponding to Invasin were collected and its absorbance spectrum was by measured at the Cary Eclipse Fluorescence spectrophotometer. Invasin concentration C and labelling ratio n^* (the labeling molar ratio of the fluorescence species) were estimated from the sample absorbance measurements A_{280} and A_{max} (absorbances at $\lambda = 280$ nm and λ corresponding to the fluorescence of the dye which for the JF549 is 549 nm), the extinction coefficients of JF549 dye ϵ_{dye} (from tocris.com) and Invasin ϵ_{prot} (expasy.org/protparam) 101000 [M^{-1} cm^{-1}] and 57995 [M^{-1} cm^{-1}] , respectively, and the CF correction coefficient that is equal to 0.169 (from tocris.com):

$C = (A_{280} - A_{max} \cdot CF)/ \epsilon_{dye}$;

$n^* = A_{280}/ \epsilon_{prot} \cdot C$.

Supported lipid bilayer (SLB) preparation

The protocol is inspired by the protocol developed in the group of Jay Groves[1,5].

The SUV solution is incubated in the sample chamber for 30 min to allow the SUV fusion on the substrate. Then the unfused vesicles are washed away with 10 x chamber volumes of the SUV fusion buffer. Next, the SLBs are washed with 10 x chamber volumes of the cell buffer: 25 mM HEPES pH 7.3; 120 mM NaCl; 7 mM KCl; 1.8 mM $CaCl_2$; 0.8 mM $MgCl_2$; 5 mM glucose. Any remaining defect on the surface is then passivated by incubation of the chamber in a "blocking" solution made of the cell buffer complemented with 0.1 mg/ml β-casein for 15 min. Then the SLBs is washed again with 10 x chamber volumes of the cell buffer to remove the excess of the blocking solution.

To prepare Invasin-coated SLBs, bilayers containing Ni-lipids are functionalized with 6xHis-tagged Invasin following the protocol[1]. SLBs are incubated with 400 nM Invasin in the cell buffer for 1 hour at room temperature. Then the unbound proteins are washed away with 10 x chamber volumes of the cell buffer in two steps spaced in time by 30 min.

SLB quality and fluidity control

We prepared RGD-SLB and SLB(Ni), functionalized SLB(Ni) with fluorescently labelled Invasin or EGFP (as a control). To assess the quality of SLBs (absence of defaults) they were inspected visually under the microscope. We observed fluorophore distributions in both DHPE-Marina-Blue and fluorescent proteins. If no defaults were detected, we proceeded further and tested the SLBs on

fluidity. The fluidity of the prepared SLBs were checked by using the fluorescence recovery after photobleaching (FRAP) technique (Figure S1A). We can deduce the diffusion coefficients of fluorescent lipids or proteins attached to the bilayer by analyzing the fluorescence recovery curves after photobleaching of a small area of the SLB[6]. For each sample we have measured 10 FRAP curves in 2 experiments from a photobleached circular zone of approximately 20 μm^2. A typical normalized fluorescence recovery curves for lipids (DHPE-Marina Blue) of the SLB(Ni) in presence of Invasin and Invasin on the SLB(Ni) are shown in the Figure S1B. They were fitted with the following function:

$$f(t) = f_0 + (f_{plateau} - f_0)(1 - e^{-kt}),$$

from which we can find the immobile fraction of fluorophores as $1 - f_{plateau}$. The interaction of the lipid bilayer with the solid surface is limited since the immobile fraction (Figure S1C) for fluorescent lipids is lower than 7% for SLB-RGD, and even lower for SLB-Ni. Lipids remain mobile when Invasin or EGFP is bound to the SLB-Ni. We also see that the immobile fraction of Invasin on the SLB is of the order of 11%, and 5% for EGFP. The diffusion coefficient D, the radius of the bleached area r and the half-recovery time $t_{1/2}$ are link by the following expression: $D = 0.224 \cdot r^2/t_{1/2}$.

The diffusion coefficients for lipids are approximately 75% lower in SLB(Ni) than in SLB(RGD), maybe due to electrostatic interactions between the glass and the Ni lipids (0.8 versus 1.4 $\mu m^2/s$, respectively) (Figure S1D). These values are in fairly good agreement with the previous studies of lipid diffusion in lipid bilayer (SLBs or liposomes)[7,8]. Binding of Invasin or EGFP to the bilayer does not change the lipid diffusion coefficient, showing that the bilayer is fluid. As expected, since proteins are bigger than lipids, the protein diffusion coefficients are lower, more than two times lower than that of the lipids (0.4 and 0.3 $\mu m^2/s$ for Invasin and EGFP respectively). These results show that the RGD-lipids and Invasin-lipids complexes in our experiments are mobile in the bilayer.

Fluorescence calibration of SLBs

The aim of the calibration is to quantify the density of fluorescence species in the cell adhesion plane by using supported lipid bilayers as fluorescence standards. We adapted the original protocol[5] to perform the calibration. Within a certain range of fluorophore densities, we can relate the density of the fluorescence species n_{fl} [μm^{-2}] and the intensity I_{fl} [AU] of the fluorescence image of the cell surface in the adhesive contact by the following:

$$N_{fl} = A_{fl} \cdot I_{fl};$$

where A_{fl} is the proportionality factor that depends on the fluorescent molecule and imaging conditions. This linear relationship holds for concentrations below the critical concentration at which fluorophores start to self-quench[9]. The range of densities of fluorescence species where this linear relationship holds is verified during the calibration process.

Standards have to be used to calibrate the fluorescence in membranes, in illumination conditions similar to the experiments. In practice, fluorescent lipids are convenient since they can be incorporated in the bilayer at controlled concentration, thus their density is known and the corresponding fluorescence can be measured as a function of their density. Here, SLBs are particularly suitable if the fluorescence intensity is measured in the exact same conditions as in the experiments where the contact zone between cells and SLBs are imaged. But, to account for differences in fluorescence yield between the fluorescent markers on the lipid and the protein, the fluorescence of the lipids and the proteins at known concentrations must be compared; for this, measurements in bulk are well-suited.

The proportionality factor A_{fl} is related to the proportionality factor of the calibration standard A_{st} by the following relation:

$A_{fl} = A_{st} / (F \cdot n^*)$;

where the correction factor $F = I_{fl}/I_{st}$ is the ratio between the intensities of the fluorescence species I_{fl} and the standard I_{st} at a given concentration in solution and n^* is the labeling molar ratio of the fluorescence species. $n^* = 1$ for lipids, but might be not equal to 1 for proteins, depending on the efficiency of the labeling protocol. n^* must be measured for each preparation of proteins with a spectrophotometer.

F considers the optical properties of the microscope and spectral differences between the fluorophore and the standard. In order to determine A_{fl} for a given fluorophore, we need to do the following:

1. Calibrate our imaging system with a standard fluorophore and measure the proportionality factor A_{st} in SLB with fluorescent lipids;

2. Measure the correction factor F with experiments in solution.

More precisely, in the first step, we prepare a series of SLBs with fluorescence lipids (standard) incorporated at known densities. Then we image these SLBs with exactly the same imaging conditions (laser powers, exposure times and fluorescence channels, or sets of fluorescence filters) as we do for the fluorophore of interest. We have taken at least 10 images in different areas of the SLB for every density of every studied fluorophore. In the second step, we measure the correction factor F, the dimensionless factor that represents the efficiency of the fluorophore versus the standard. Practically, to calculate F, we measure the ratio of intensities between the fluorophore and the standard at a given concentration in solution (in bulk), or more precisely, the ratio of the slope of the plots Intensity versus bulk concentration, for both fluorophores, α_{st} and β_{fl}. This measurement must be done directly at the microscope with exactly the same imaging conditions as for the first step. We did 2 calibrations (in green and red channel) for the following molecules: AlexaFluor488 and JF549.

We used Bodipy FL DHPE (Molecular probes, referred to as BodipyFL in the following) and Texas Red DHPE (Invitrogen, referred to as TexasRed in the following) lipidated dyes as standards for the green and the red calibrations, respectively.

Fluorophore preparation for calibration

All fluorophores, except the lipidated ones, were diluted in the working cell buffer (25 mM HEPES pH 7.3; 120 mM NaCl; 7 mM KCl; 1.8 mM $CaCl_2$; 0.8 mM $MgCl_2$; 5 mM glucose). As lipids would aggregate in aqueous solution, we have solubilized them in detergent. Lipid solutions of BodipyFL or TexasRed were blow-dried under argon and vacuum for 30 minutes, and re-solubilized in the working cell buffer with 2.25 mM n-Dodecyl β-D-maltoside (DDM, Sigma Aldrich).

The accuracy of the calibration greatly relies on the precise knowledge of the fluorophore concentrations. The concentrations of all samples were checked on Cary Eclipse Fluorescence Spectrophotometer using the following published extinction coefficients: AlexaFluor488 (73000 [$M^{-1}cm^{-1}$]), BodipyFL (80000 [$M^{-1}cm^{-1}$]), JF549 (101000 [$M^{-1}cm^{-1}$]), TexasRed (116000 [$M^{-1}cm^{-1}$]), mCherry (72000 [$M^{-1}cm^{-1}$]).

The images of the fluorophores in bulk were taken approximately 10 µm above the coverslip. We observed that the intensity distribution of the fluorescence signal of a dye in solution is not homogenous in the imaging plane (Supplementary Fig. S3). This is related to the non-homogeneous illumination. The illumination seems to be more or less homogeneous in the middle of the illumination pattern “the plateau” (Supplementary Fig. S3A). For our analysis we either considered the intensity in this region or corrected the inhomogeneity of the illumination by using the fluorescence signal of bilayers. We have taken at least 10 images in different areas of the chamber for every concentration of every studied fluorophore.

The standard SLBs (DOPC + BodypyFL) with different concentrations of BodipyFL were prepared following the previously described protocol ("SLB preparation" in the Methods). We calculated the surface densities of BodipyFL in the SLBs from their molar ratios and assuming the area of a DOPC lipid projected on the SLB plane to be 0.72 nm^2 and, thus, the number of lipids per μm^2 to be $2 \cdot \mu m^2 / 0.72\ nm^2 = 2.8 \cdot 10^6$ (where the factor 2 is to take both bilayer leaflets into account)[10]. For each sample 30 images were taken and the intensities of the plateau region were averaged. We plotted the density-intensity standard curves for both calibrations and also intensity-concentration curves for all fluorophores in bulk (Supplementary Fig. S3). Therefore, we obtained the following calibration values for our fluorescence species:

β_1-integrin labelled with Alexa Fluor 488 (A_st = 3.146 μm^{-2}; alpha_fl = 3410 μM^{-1}; beta_st = 1872 μM^{-1}; F = 1.82; n* = 1; A_fl = 1.73 μm^{-2});

JF549 labelled Invasin (A_st = 3.857 μm^{-2}; alpha_fl = 2366 μM^{-1}; beta_st = 1167 μM^{-1}; F = 2.03; n* = 0.427; A_fl =4.45 μm^{-2}).

Note that the calibration factors were measured from fluorescent dyes in solution and not from fluorescent proteins. F was shown to be about 3 times higher with AlexaFluor488 bound to anti-biotin than to Streptavidin[5]. But, weaker differences were observed in other cases. In practice, we should purify the proteins of interest, label them and make the calibration, which is not possible. In addition, it is possible that the dye fluorescence is different in the cell environment as compared to the buffer. Thus, the absolute values of the protein densities in the adhesion structures that we deduce from our experiments might be off by some systematic factor, however, it cannot be by an order of magnitude.

According to the fluorescence calibration we found that Invasin was distributed homogeneously on SLBs and its density corresponded to approximately 600 Invasin/μm^2 (under our SLB preparation protocol).

Microscopy

We have used a spinning disk microscope to image fluorescent lipid bilayers and cell adhesion on them. The microscope consists of a CSU-X1 Yokogawa head mounted on an inverted Ti-E Nikon microscope with a motorized XY stage (MadCity Lab®). Images were acquired with Metamorph software (Molecular Devices®) through a 100x NA1.45 objective with a Photometrics 95B-sCMOS camera. Live cell adhesion imaging was performed at 30°C using the stage top incubator (Tokai hit®). Fixed cells were imaged at RT with the same microscope. The setup is equipped with 4 Cobolt lasers from Hübner Photonics: 405 nm (100mW), 488 nm (100mW), 561 nm (50mW) and 633 nm (100mW). They allow sample imaging in 4 fluorescence channels (405, GFP, Cy3 and Cy5). Samples can also be imaged in wide field mode using the transmission light from LED source. The setup is also equipped with a FRAP photoactivation module.

We have used the same imaging conditions in our microscopy experiments: 405 (laser power: 15%; exposure time: 100ms), GFP (laser power: 30%; exposure time: 300ms), Cy3 (laser power: 30%; exposure time: 300ms) and Cy5 (laser power: 30%; exposure time: 300ms).

For imaging cells above the bilayer Z-stack images of 3 µm height are taken. The stack is centered at the SLB plane and its step is 0.3 µm.

Diffraction limit (DL), or optical lateral (xy plane) resolution was calculated as follows:

$Res_{xy} = 0.51 \cdot \lambda_{em} / NA$,

Where λ_{em} – emission wavelength of a fluorophore, NA – numerical aperture of the objective.

Image analysis

- **"trembling/adherent" cells**

Cells were qualitatively classified as "trembling" if their edges but not their centers of mass moved at the time scale of 5 seconds. The edge movement was detected manually based on the bright field images.

- **Cell contour detection and measurement of cell morphology parameters**

Cell contours were manually detected from bright field images by using a polygonal selection tool in ImageJ. Then the "cell contour" selection was used to calculate the projected cell area A ("projected area") and the cell circularity index C ("circularity") as follows:

$C = 4pi*A/P^2$, where P is the perimeter of the "cell contour" selection.

- **Integrin cluster detection and quantification**

Before detecting integrin clusters, we made a correction on the illumination inhomogeneity. The illumination is not homogeneous across the image (Supplementary Fig. S3A). Therefore, we introduced the "illumination" map to correct this issue. It consists in normalizing the image by that of a fluorescent supported lipid bilayer (SLB). The SLB has a homogeneous distribution of fluorescent lipids in the image plane, so it is a perfect candidate for the illumination map. The intensities of the illumination map range between 0 (the dimmest illumination) and 1 (the brightest illumination). Therefore, the image correction for the illumination inhomogeneity is obtained by the division of pixels intensities of the image by the intensities of the corresponding pixels of the illumination map.

To detect β_1-integrin clusters we first used previously described fluorescence calibration transforming raw intensity images of integrins (corrected for illumination inhomogeneity) to integrin concentration maps. Second, we segmented these concentration maps by defining an integrin density threshold that separates two distributions (clusters and background) on the density histogram. The integrin density thresholds could be set manually or automatically by using an algorithm based on Renyi's entropy thresholding. This thresholding method was previously described[11] and is now one of the standard threshold methods available in ImageJ. The method defines a threshold intensity value that maximizes the informational entropy and entropic correlation of "cluster" and "background" distributions[12].

Custom-written code used to analyze the data in the current study is available from the corresponding authors on reasonable request.

FA protein, actin and microtubule enrichments in β_1-integrin clusters

Signal enrichment of the co-expressed fluorescent fusion proteins (FPs) for FA proteins, F-actin and microtubule imaging at β_1-integrin clusters was calculated as follows. Mean fluorescence intensity of the FP was detected in the region of β_1-integrin clusters and then was normalized by the mean intensity of the FP in the cell. It was compared with "shuffled control enrichments", enrichment calculated at random pixels instead of β_1-integrin clusters regions.

FA protein recruitment to integrin clusters experiments were done in fixed cells. Fluorescence calibrations were not performed in these conditions. β_1-integrin clusters were defined using the same threshold (100 AU).

β_1-integrin clusters were defined using the threshold of 100 integrins/μm^2 for experiments of F-actin and microtubule recruitment to integrin clusters.

Cell culture

We used the following cell lines in our experiments:

Mouse Embryonic fibroblasts (MEF) β_1KO β_1-Halotag and MEF β_1KO β_1-Halotag paxillin-mCherry (both gifts from David Calderwood, Yale University). The former cell line was constructed by lentiviral transfection of a β_1KO MEF cell line with an ecto-tag construct based on pLENTI expression vector and the latter as a consecutive lentiviral transfection with a paxillin-mCherry on pLENTI expression vector. The Halotag sequence was inserted on an exposed loop (β_1 residues 91-114)[13].

MEF β_1KO β_1-Halotag LifeAct-mScarlet that was constructed by lentiviral transfection of a β_1KO β_1-Halotag MEF cell line with a LifeAct-mScarlet on pLVX expression vector.

MEF β_1KO β_1-Halotag EMTB-iRFP that was constructed by lentiviral transfection of a β_1KO β_1-Halotag MEF cell line with an EMTB-iRFP on pLVX expression vector (gift from Simon De Beco, Paris Diderot University).

HeLa WT and HeLa β_1-Halotag that we constructed by lentiviral transfection of a HeLa WT cell line with an ecto-tag construct based on pLENTI expression vector (gift from David Calderwood, Yale University).

MEF and HeLa cells were cultured in Dulbecco's Modified Eagles Medium (DMEM) high glucose + GlutaMAX (Thermo Fischer Scientific) supplemented with 10% fetal bovine serum (FBS; EuroBio) and 1% penicillin-streptomycin (Thermo Fischer Scientific). Cells were cultured at 37°C in a humidified 5% CO_2 atmosphere. Cells were routinely monitored for mycoplasma contamination following a well-established PCR-based method (Young et al. [2010]) and found to be negative.

DNA plasmids

For transient cell transfections the following plasmids were used: talin-mCherry (Addgene plasmid # 55137), vinculin-mCherry[14], VASP-mCherry (Addgene plasmid # 55151), kindlin-2-mCherry (gift from Christof Hauck, Konstanz University), zyxin-mCherry (gift from Danijela Vignjevic, Institut Curie).

For lentiviral transfections the following plasmids were used: β_1-Halotag (gift from David Calderwood, Yale University), pLVX EMTB-iRFP (gift from Simon De Beco, Paris Diderot University) and pLVX LifeAct-mScarlet.

The pLVX LifeAct-mScarlet plasmid was prepared in two steps: a polymerase chain reaction using 5'-TCTAGAGCTACTAACTTCAGCCTGCTG-3' / 5'- CGGTGGATCCCCTTCTTCC-3' primers on Ibidi USA 60101 LifeAct-GFPtag2 plasmid was cloned with In-Fusion HD enzyme kit (Takara) into the pLVX vector (Clontech) digested with Not1 and BamH1 restriction enzymes (New England Biolabs). It was followed by a second In-Fusion HD cloning of a polymerase chain reaction using 5'-GAAGGGGATCCACCGATGGTGAGCAAGGGCGAGG-3' / 5'-TTAGTAGCTCTAGACTTGTACAGCTCGTCCATGCC-3' (mScarlet insert) using BamHI and XbaI (New England Biolabs).

Cell transfections (transient by electroporation and stable lentiviral)

Transient cell transfections were performed by electroporation following the protocol adapted from Gautreau et al., 2000: trypsinized cells were resuspended at a concentration of 2.5×10^7 cells/ml in 15 mM Hepes, pH 7.4, buffered medium. 200 µl of cell suspension was added to 50 µl of a solution containing 210 mM NaCl, 5 µg of plasmid DNA, and 30 µg of salmon sperm DNA carrier (Sigma Aldrich). Then cells were electroporated with a BioRad Gene Pulser at 950 µF and 240 V using 4-mm width cuvettes. Transiently transfected cells were analyzed after 48 h of the expression of the plasmid of interest.

Stable cell transfections were performed with lentiviral infections. Lentiviral particles (LVs) were produced in HEK 293T cells cultured in Dulbecco's Modified Eagle's Medium (Thermo Fisher Scientific), supplemented with 10% Fetal Bovine Serum (EuroBio) and 1% Pen/Strep + 1% Sodium Pyruvate + 1% Non-Essential Amino Acids solution (Gibco) at 37°C in 5% CO_2 humidified incubators. Cells were plated the day before transfection in T75 flasks (approx. 6 million) to achieve a 50–70% confluency the next day. Plasmids coding lentiviral components, pPAX2 (Gag-Pol-Hiv1) and pMDG2 (VSV-G), and the plasmid of interest at a ratio of 4:1:4 (µg), respectively, were transfected using PEI MAX 40k transfection reagent (Tebu-Bio) according to the manufacturer's protocol. After 48 hrs, LVs were concentrated using a 100k Amicon column (Merck Millipore) and the pellet was resuspended up to 400 µL in PBS. MEF or HeLa cells were plated the day before infection in 6-well plates (approx. 100,000 cells) to achieve a 50–70% confluency the next day. Cells were transduced with 100 µL of the desired LVs, for 72 hrs. After transduction, expressing cells were treated with 2 µg/mL puromycin. Positive cells were sorted using a SH800 FACS Cell Sorter (Sony).

Integrin labeling and cell seeding in imaging chambers

Cultured cells were serum starved for 24 hours before experiment. Then cells were detached by Versene solution (Sigma Aldrich) for 30 minutes at 37°C. Then they are incubated with an Alexa Fluor488 Halotag® ligand (Promega) (400 nM per 1 ml containing approximately 1.5-2 million cells) to label β_1-integrin-Halotag for 10-15 minutes at room temperature. Then cells are span down at low centrifuge speed (1000 rpm in Megafuge 16R centrifuge from Thermo Scientific), resuspended in the cell buffer (25 mM HEPES pH 7.3; 120 mM NaCl; 7 mM KCl; 1.8 mM $CaCl_2$; 0.8 mM $MgCl_2$; 5 mM glucose) to remove the Versene and the excess of dye and filtered with Falcon 40 µm Cell Strainer (Corning) to remove cell clumps. Cells then were gently flown into the imaging chamber containing SLBs. The chamber is then sealed with mineral oil (M8410, Sigma Aldrich).

Since our aim was to study mechanosensitive aspects of cell adhesion, we avoided washing steps in chambers once cells were seeded. Indeed, flows in the chamber exert shearing forces on adhering cells that can reinforce cell adhesion[15].

Buffers, reagents, inhibitors

The following cell buffer was used in imaging experiments: 25 mM HEPES pH 7.3; 120 mM NaCl; 7 mM KCl; 1.8 mM $CaCl_2$; 0.8 mM $MgCl_2$; 5 mM glucose.

SiR-tubulin (Cytoskeleton, Inc.) at the dilution suggested by the manufacturer was used to label microtubules in live cells.

In the experiments with manganese-treated cells, $MnCl_2$ (Sigma Aldrich) was added (to the final 0.5mM concentration) just before putting cells into the imaging chamber.

We used the following concentrations of inhibitor drugs in this study: 50 µM for the Arp2/3 complex inhibitor CK-666, 10 µM for the formin inhibitor SMIFH2 (Sigma Aldrich), 50 µM for the myosin inhibitor *p*-nitro-Blebbistatin (Cayman Chemical), 50 µM for the ROCK inhibitor Y27631 (Sigma Aldrich), 10 µM for Nocodazole (Sigma Aldrich) and 50 µM for the cytoplasmic dynein inhibitor Ciliobrevin D (Sigma Aldrich). For the live cell imaging experiments drugs were added at the same moment as cells were seeded to chambers. Control samples were treated with an equivalent amount of DMSO which did not exceed 0.001% v/v.

Immunofluorescence

For endogenous ELKS and KANK1 labeling, MEF cells were fixed in 100% ice-cold methanol (−20 °C, 5 min) followed by incubation in PBS with 1 mg ml^{-1} BSA (blocking buffer (BB)) all along the procedure. Fixed cells were washed in PBS and saturated in BB. Cells were incubated with the primary antibody (rabbit anti-ELKS[16], 1:200, or rabbit anti-KANK1, Atlas antibodies, HPA005539, 1:200) diluted in BB (45 min), washed three times in BB, and incubated with the anti-mouse secondary antibody conjugated to Alexa Fluor 555 (Invitrogen) for 30 minutes. Cells were washed twice in BB, once in PBS and once in dH_2O. Finally, coverslips were mounted in Abberior mounting medium (Abberior) and examined under fluorescence microscope.

siRNA interference

The sequences of siRNA for p150Glued are obtained from Eurogentec: GGUAUCUGACACGCUCCU and UAGGAGCGUGUCAGAUAC. Non-targeting siRNA ON-TARGETplus (D-001810-10-05) (Dharmacon, GE Healthcare) served as the siRNA control ("siRNA scramble"). siRNA transfection was performed using Lipofectamine RNAiMAX transfection reagent (Thermo Fischer) at a final concentration of 40nM for 48 hrs prior to cell imaging. Protein knock down efficiency was confirmed by real-time quantitative PCR and Western Blot analysis (Supplementary Fig. S6C).

Western Blot analysis

Western blots were performed on protein extracts of siRNA silenced HeLa to estimate the degree of knockdowns of Dynactin (p150glued) (Supplementary Fig. S6C). siRNA silenced Dynactin (p150glued) HeLa cells were resuspended in RIPA Buffer (50 mM TRIS pH8.0, 150 mM NaCl, 1% NP-40, 0,1% SDS) supplemented with cOmplete protease inhibitor cocktail (Roche). Sample was centrifuged at 20,000 *x g* for 1 min and protein supernatant were collected and concentrations checked with Bradford assay. 100 µg of each sample was run on a 4-12% NuPAGE Gel, which was then transferred onto a PVDF membrane using the BioRad Trans-Blot Turbo system. Membranes were blocked in 5% Milk, TBST and treated with p150glued Antibody (Mouse, BD biosciences) or ß-actin (Mouse, Genetex) as the loading control at a 1:1000 dilution in TBS-T at 4°C overnight, then the secondary Goat-anti-mouse HRP antibody (Sigma Aldrich) at 1:10 000 dilution in TBS-T, for 1h. Pierce™ ECL 2 Western Blotting Substrate (Thermo Scientific Kit) was added and blots developed using the Amersham Imager AI 680. To assess the degree of siRNA silencing of p150glued we quantified the relative change in the protein expression, using the Fiji "Measure" plugin and using the same region of interest (ROI) across the bands in one blot normalized by the intensity of the appropriate β–actin band (indicates the amount of loaded protein).

Statistical analysis

Statistical analysis was performed in GraphPad Prism. $P<0.05$ was considered statistically significant. At least three experiments were performed in order to conduct a statistical test (number of experiments are indicated as Nexp in the figure captions). Data sets were tested with the D'Agostino and Pearson normality tests. Normally distributed data sets were analyzed with Student's t tests or with one-way ANOVA Tukey tests if they contained two or more conditions respectively. Data sets with non-normal distributions were analyzed with a Kruskal–Wallis test (multiple comparison) or Wilcoxon rank sum test (two-sample comparison).

Bibliography (methods)

1. Nye, J. A. & Groves, J. T. Kinetic Control of Histidine-Tagged Protein Surface Density on Supported Lipid Bilayers. *Langmuir* **24**, 4145–4149 (2008).
2. Humphries, J. D., Byron, A. & Humphries, M. J. Integrin ligands at a glance. *J. Cell Sci.* **119**, 3901–3903 (2006).
3. Van Nhieu, G. T. & Isberg, R. R. The Yersinia pseudotuberculosis invasin protein and human fibronectin bind to mutually exclusive sites on the alpha 5 beta 1 integrin receptor. *J. Biol. Chem.* **266**, 24367–24375 (1991).
4. Leong, J. M., Fournier, R. S. & Isberg, R. R. Identification of the integrin binding domain of the Yersinia pseudotuberculosis invasin protein. *EMBO J.* **9**, 1979–1989 (1990).
5. Galush, W. J., Nye, J. A. & Groves, J. T. Quantitative fluorescence microscopy using supported lipid bilayer standards. *Biophys. J.* **95**, 2512–2519 (2008).
6. Soumpasis, D. M. Theoretical analysis of fluorescence photobleaching recovery experiments. *Biophys. J.* **41**, 95–97 (1983).
7. Guo, L. *et al.* Molecular Diffusion Measurement in Lipid Bilayers over Wide Concentration Ranges: A Comparative Study. *ChemPhysChem* **9**, 721–728 (2008).
8. Pincet, F. *et al.* FRAP to Characterize Molecular Diffusion and Interaction in Various Membrane Environments. *PloS One* **11**, e0158457 (2016).
9. Dahim, M. *et al.* Physical and photophysical characterization of a BODIPY phosphatidylcholine as a membrane probe. *Biophys. J.* **83**, 1511–1524 (2002).
10. Nagle, J. F. & Tristram-Nagle, S. Structure of lipid bilayers. *Biochim. Biophys. Acta* **1469**, 159–195 (2000).
11. Kapur, J. N., Sahoo, P. K. & Wong, A. K. C. A new method for gray-level picture thresholding using the entropy of the histogram. *Comput. Vis. Graph. Image Process.* **29**, 273–285 (1985).
12. Sahoo, P., Wilkins, C. & Yeager, J. Threshold selection using Renyi's entropy. *Pattern Recognit.* **30**, 71–84 (1997).
13. Huet-Calderwood, C. *et al.* Novel ecto-tagged integrins reveal their trafficking in live cells. *Nat. Commun.* **8**, 570 (2017).
14. Valencia-Gallardo, C. *et al.* Shigella IpaA Binding to Talin Stimulates Filopodial Capture and Cell Adhesion. *Cell Rep.* **26**, 921-932.e6 (2019).
15. Riveline, D. *et al.* Focal contacts as mechanosensors: externally applied local mechanical force induces growth of focal contacts by an mDia1-dependent and ROCK-independent mechanism. *J. Cell Biol.* **153**, 1175–1186 (2001).
16. Monier, S., Jollivet, F., Janoueix-Lerosey, I., Johannes, L. & Goud, B. Characterization of Novel Rab6-Interacting Proteins Involved in Endosome-to-TGN Transport. *Traffic* **3**, 289–297 (2002).